ISSN 1849–0751 (On–line)
ISSN 0013–7448 (Print)
UDK 621.31

Journal of Energy

VOLUME 68 Number 4 | 2019 Special Issue

ENERGIJA

Journal of Energy

Scientific Professional Journal Of Energy, Electricity, Power Systems

Online ISSN 1849–0751, Print ISSN 0013–7448, VOL 68

Published by

HEP d.d., Ulica grada Vukovara 37, HR–10000 Zagreb

HRO CIGRÉ, Berislavićeva 6, HR–10000 Zagreb

EDITORIAL

Journal of Energy special issue: Papers from 5th International Colloquium "Transformer Research and Asset Management" – Numerical Methods

Welcome to this special issue, which is based on selected papers presented at the 5th International Colloquium "Transformer Research and Asset Management", held in Opatija, Croatia, on October 9th-12th, 2019.

The International Colloquium was organized by the Croatian CIGRÉ National Committee in cooperation with the Faculty of Electrical Engineering and Computing in Zagreb and the Centre of Excellence for Transformers in Zagreb with support from CIGRÉ A2 Study committee (Transformers). The goal of the Colloquium was to share latest research in the in the areas of distribution, power and instrument transformers. The Colloquium extended over three days. Participants from manufacturers, utilities and universities took part in discussions.

All the papers were divided into three sessions

Numerical Modeling
- Electromagnetic field
- Coupled fields
- Transients
- Numerical modeling in design, etc.

Materials, Components and New Technologies
- Insulating material
- Magnetic material and transformer noise
- Transformer components
- Digitalization and smart grids
- Transformer new technologies, etc.

Transformer Life Management
- Diagnostics, monitoring and failures
- Resilience
- • Asset management
- In-service experiences, etc.

We would like to thank the authors for their contributions and the reviewers who dedicated their valuable time in selecting and reviewing these papers. We hope this special issue will provide you a valuable source of newest achievements in transformer technology.

Guest Editors

asst. prof. dr. sc. **Žarko Janić**
Končar Power Transformers
A joint Venture of Siemens AG and Končar d.d.

ass. prof. dr. sc. **Bojan Trkulja**
University of Zagreb, Croatia
Faculty of Electrical Engineering and Computing

Journal of Energy

VOLUME 68 Number 4 | 2019 | Special Issue

journal homepage: http://journalofenergy.com/

Numerical Computation of the Vibroacoustic Behaviour of an Oil-Immersed Power Transformer

Bruno Bosnjak, Dariusz Nowak, Sever Michalowski
Hyundai Electric Switzerland AG, Zürich, Switzerland
E-mail: bruno.bosnjak@hyundai-electric.ch

***Abstract*— This paper presents a numerical calculation method that allows for the simulation of the mechanical and acoustic behaviour of a transformer tank. In order to simulate the vibroacoustic behaviour of an oil-immersed power transformer, an acoustic-mechanical coupled three-dimensional finite-element method model of a transformer was setup. The simulation is performed in the frequency domain at frequencies adjacent to the driving frequency. A vibration source closely resembling the actual active part of the transformer is placed within the oil-filled tank that mechanically represents an acoustic cavity with flexible steel boundaries. Via a fluid-structure interface the vibration source generates acoustic waves in the oil medium which partly transmit through the tank wall structure and partly reflect within the steel transformer tank again via a fluid-structure interface. The vibrating tank is then coupled with the external acoustic air medium and the corresponding sound field is calculated and evaluated according to IEC 60076-10. This numerical computation allows for the direct calculation of the complete vibrational and acoustic behaviour of a transformer.**

***Index Terms*— Power Transformer Noise, Finite Element Method, Multiphysics, Vibration, Tank**

I. INTRODUCTION

The noise emitted by power transformers is generally unpleasant for nearby residents and increasing urbanization go hand in hand with the increasing energy needs of the population. In order to protect the general population from adverse effects of continuous exposure to noise, the local and national legislations in the developed countries limit the amount of noise emitted into the environment by power transformers (such as [1]). Therefore, it is important to accurately calculate and predict the noise emitted by a transformer in operation on order to satisfy the customer requirements and to stay within the legislative limits. This paper focuses on the numerical analysis of the vibroacoustic behavior of a power transformer in operation, namely during a short circuit test with 100% of nominal current flowing through the transformer windings. Coupled numerical simulations provide a powerful tool for the optimization of the tank during transformer design phase with respect to low noise emissions.

II. TRANSFORMER NOISE

Power transformers are a source of low frequency tonal noise during operation. Power transformer noise can be divided into three components according to the point of origin and noise generation mechanism – core noise (no load noise), winding noise (load noise) and cooling system noise.

The core noise is, to a great degree, caused by magnetostrictive core vibrations originating from oscillatory magnetic fields in the core. Maxwell force acting between the electrical steel sheets of the core also contribute to the noise generation, albeit to a smaller degree than magnetostriction. Since magnetostriction acts unidirectionally, the generated core noise has tonal components at twice the line frequency and at even higher harmonics thereof.

Winding noise is generated by winding vibrations caused by Lorentz forces acting on the transformer windings in load conditions. Due to the imperfect magnetic coupling of the windings, a stray magnetic flux is generated between the transformer windings. The interaction of the stray magnetic flux and the current-carrying conductors of the windings leads to the generation of Lorentz forces that also act unidirectionally generating noise at twice the line frequency.

Fans and pumps of the transformer cooling system generate a broadband noise typical for forced flow of air or oil. Usually, the cooling system noise is lowered by reducing the speed of the fans and therefore reducing the air flow. Reduced air flow in the fans lowers the cooling performance of the system and increases the number of fans necessary to achieve the required cooling performance [2].

The total sound power level of a transformer at certain load conditions is given by the logarithmic sum of these three sound power components at defined load conditions [3].

III. GOVERNING EQUATIONS

Numerical calculations of the vibroacoustic behavior of an oil immersed power transformer must consider the interaction between the magnetic, mechanical and acoustic physical domain. Since the focus of this paper is on the vibroacoustic properties of the transformer tank, the magnetic domain is omitted from this consideration. The vibrations caused by the magnetostriction, Maxwell forces and Lorentz forces are directly measured on an actual transformer unit and set as the initial conditions in the vibroacoustic simulation.

For the mechanical field in the solid, the materials used are considered to have linear elastic and isotropic properties. Therefore, their dynamic behavior can be described using the following partial differential equation[4]:

$$\frac{E}{2(1-\nu)}\left((\nabla\cdot\nabla)\vec{d}+\frac{1}{1-2\nu}\nabla(\nabla\cdot\vec{d})\right)+\overrightarrow{f_V}=\rho\frac{\partial^2\vec{d}}{\partial t^2} \tag{1}$$

where E is the modulus of elasticity, ν is the Poisson's ratio, ρ is the material density, f_v is the volumetric force and d is the mechanical displacement. As for the acoustic wave, assuming a homogenous, non-viscous fluid, its' propagation is governed by the linear wave equation[5]:

$$\nabla^2 p=\frac{1}{c^2}\frac{\partial^2 p}{\partial t^2} \tag{2}$$

where p is the acoustic pressure and c sound velocity in the fluid. The acoustic pressure can be calculated using the scalar velocity potential ψ as follows:

$$p=\rho\frac{\partial\psi}{\partial t}. \tag{3}$$

These two domains are then coupled at the fluid-structure interface, where the condition that the normal component of particle velocity $\partial\psi/\partial n$ in the fluid must be equal to the normal component of the surface velocity v_n of the solid at the fluid-structure interface. Therefore, the following condition must be satisfied at the fluid-structure interface in order for the two domains to interact:

$$v_n=\vec{n}\cdot\left(\frac{\partial\vec{d}}{\partial t}\right)=-\vec{n}\cdot\nabla\psi=-\frac{\partial\psi}{\partial n} \tag{3}$$

IV. MEASUREMENT ON A 18MVA TRANSFORMER

The vibrations of the tank and the active part of a three phase 18MVA transformer were measured during operation. All measurements were performed using a laser Doppler vibrometer. The measurement equipment allows only for measurement of the vibration in the plane directly perpendicular to the laser beam. Strictly speaking, the laser beam impinges on the surface of the object at angle slightly different than 90º. Therefore, the normal of the local surface and the direction of the laser beam are not parallel. This introduces a certain amount of error to the measurement which is typically negligible with the increasing distance from the measured object due to the reduction of the parallax angle. The distribution of the measurement points on the active part of the transformer can be seen in Figure 1.

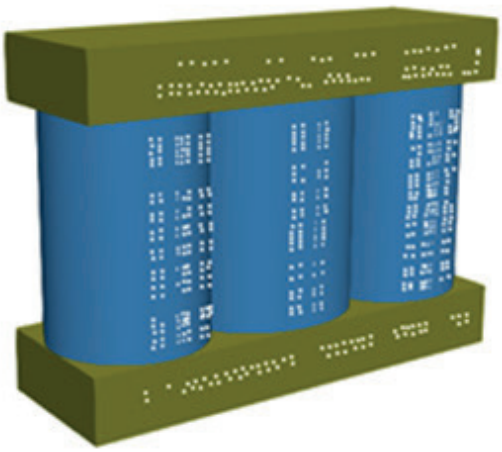

Figure 1 Distribution of measurement points on the active part

The measured displacements and velocities in the measured positions were used as basis for the calculation of the actual vibrations of the active part immersed in oil.

The measurement of the tank vibrations was performed during a short-circuit test load condition with the 100% of the load current in the windings. The scanning point were uniformly distributed on the transformer tank plates as shown in Figure 2.

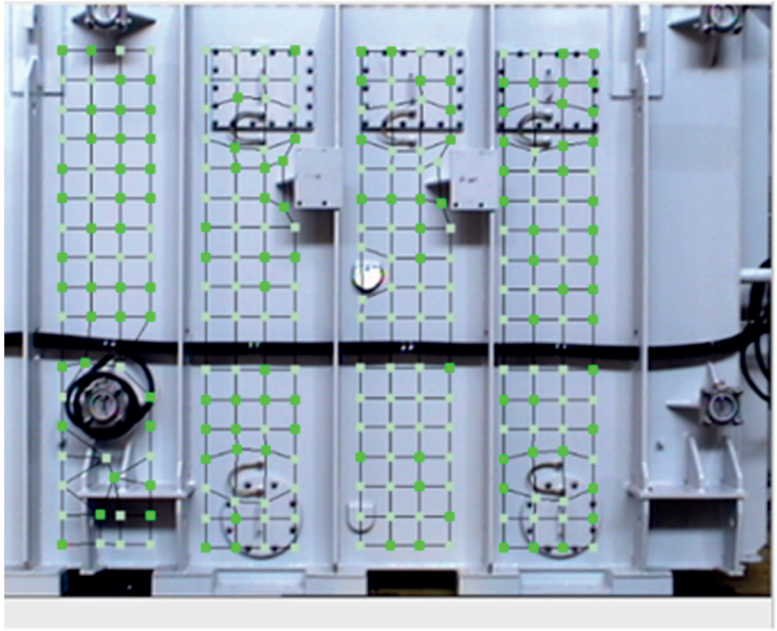

Figure 2 Distribution of the scanning points on the transformer tank

Certain areas of the tank had to be omitted from the measurement since they were covered in cables, pipes, flanges and other equipment and supporting structures present on the tank wall which are necessary for the functioning of the transformer. Figure 3 shows the actual measurement setup during the measurement procedure.

Figure 3 Measurement of the vibration of the transformer tank

V. NUMERICAL VIBROACOUSTIC MODEL OF A TRANSFORMER

Using the measured vibrations of the active part of the transformer, actual vibrations of the active part immersed in oil (as opposed to the active part in air) are calculated using a simplified 3D coupled model of the active part of transformer. The calculated displacements of the oil-immersed active part are then taken as the mechanical excitation in a 3D finite-element coupled acoustic-mechanic model of the transformer active part, oil, tank and the surrounding air. The phase separation of the each of the three limbs in considered by separating them in phase by 120º. The fluid-structure interfaces between the two domains (core – oil – tank wall – air) allow for the interaction of two domains and the transmission of incident vibration in the mechanical domain and sound pressure in the acoustical domain. Boundary condition in the acoustic domain is a perfectly matched layer (PML) of elements which employs additive dissipative terms in each element of the layer that attenuate outgoing waves exponentially, therefore effectively providing free field conditions at the boundary [6][7]. A slice of the 3D FEM model is shown in Figure 4.

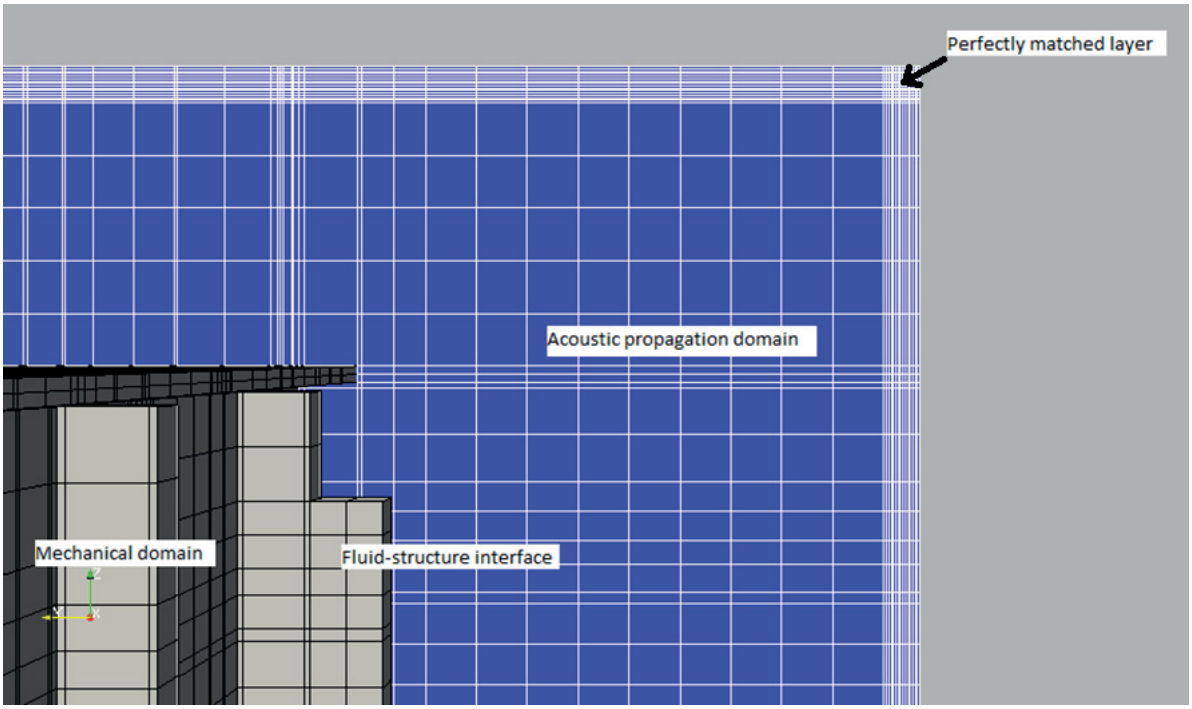

Figure 4 Slice of the vibroacoutic 3D FEM model

The simulation uses a direct solver where both the acoustical and the mechanical domain are solved simultaneously, within one matrix [7]. The surrounding floor is acoustically modeled as perfectly reflecting. The complete domain is discretized using a structured mesh in order to ensure high quality element shapes needed to avoid artificial numerical stiffening which might stem from inadequate mesh quality [7]. Since we are observing a transformer in short-circuit conditions where, for 50Hz transformers, the dominant vibration source is the 100Hz component, the frequency domain simulation is performed only for this 100Hz frequency. The finite-element model consisted of approximately 1,200,000 three dimensional finite elements.

VI. SIMULATION RESULTS

Performing the calculation, we can obtain the complete vibroacoustic behavior of the transformer tank. This includes the mechanical and acoustic interaction inside the tank, on the tank and in the surrounding air. The measured velocities of the tank vibration acquired using a 3D scanning Doppler vibrometer can be seen in Figure 5. The corresponding simulation of the vibration of the transformer tank plates can be seen in Figure **6**.

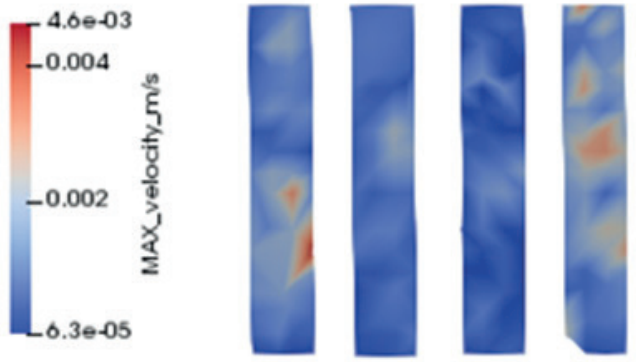

Figure 5 Measured vibration of the tank plates acc. to Figure 2

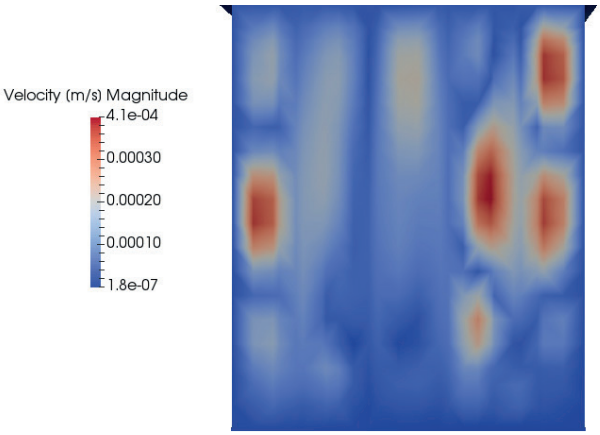

Figure 6 Simulated vibration of the tank plates at 100Hz

Comparing the two vibration forms, there are similarities in the distribution and the magnitude of the two vibration forms. The measured and simulated tank accelerations are similar, even though the exact operational deflectional shape modes do not correspond precisely. This is due to a multitude of factors influencing the vibrational behavior and the measurement such as the mechanical connection of the tank to ground, influence of the measurement setup and temperature as described in [8].

VII. CONCLUSION

The vibroacoustic behaviour of the transformer tank that was simulated generally follows the vibration form measured using a laser Doppler vibrometer and it can be sufficiently sophisticated to show general trends and vibrational tendencies of a particular transformer tank. The phase relationships in the simulated model broadly correspond to the measured ones. The scope of these investigations is generally limited to qualitative analysis since the actual amplitude of the vibration varies with other parameters that influence the vibration with influence the noise which cannot be completely described within a model or are not practically feasible to be calculated in a reasonable amount of time. Advancing these types of simulations by implementing them in the time domain does not seems feasible since a steady-state solution within a simulation is extremely time-consuming to achieve with the current state of art. Nonetheless, this simulation allows for an in-depth analysis of the interactions of the active part, oil and the tank. This allows for the optimization of the vibrational behaviour of a transformer tank by implementing mechanical changes with the general aim of reducing vibration of tank and consequently the noise emitted by the transformer.

VIII. REFERENCES

[1] Gesetz zum Schutz vor schädlichen Umwelteinwirkungen durch Luftverunreinigungen, Geräusche, Erschütterungen und ähnliche Vorgänge (Bundes-Immissionsschutzgesetz - BImSchG)

[2] T. Stirl, J. Harthun, F. Hofmann "New Trends in Noise Reduction of Power Transformers", CIRED 21st International conference on Electricity Distribution, Frankfurt 2011, Paper 0086

[3] International Standard IEC 60076-10:2016 Power Transformers – Part 10: Determination of sound levels

[4] F. Ziegler, 1991, *Mechanics of Solids and Fluids*, Springer-Verlag, Vienna

[5] G. S. Kino, 1987, *Acoustic Waves: Devices, Imaging, and Analog Signal Processing*, Prentice-Hall, Englewood Cliffs

[6] Q. Qi, T. L. Geers "Evaluation of Perfectly Matched Layer for Computational Acoustics" *Journal of Computational Physics*, Vol. 139, No. 1, January 1998, 166-183

[7] M. Kaltenbacher, 2007, *Numerical Simulation of Mechanical Sensors and Actuators,* Springer, Berlin, Germany, 139-235

[8] A. Hackl, P. Hamberger "Investigation of Surface Velocity Pattern of Power Transformers Tanks", *2010 International Conference on Electrical Machines*, Rome, Italy

Journal of Energy
VOLUME 68 Number 4 | 2019 | Special Issue
journal homepage: http://journalofenergy.com/

Measurement of Circulating Currents in Split-Winding Transformer and Comparison with Numerical Calculation

Leonardo Štrac, Juraj Haramustek, Matej Dorešić, Davor Švarc[1], B. Jurišić[2]
[1]Končar – Power Transformers Ltd., J. Mokrovića 12, 10090 Zagreb, Croatia
[2]Končar Electrical Engineering Institute, Fallerovo šetalište 22, 10000, Zagreb, Croatia
E-mail: leonardo.strac@siemens.com

***Abstract*—Split-winding transformer is a one of the common transformer types with one low-voltage winding placed above the other low-voltage winding and with the jointly high-voltage and regulation winding. The paper investigates circulating currents that occur in high-voltage and regulation windings in case of nonsymmetric load. In addition, measurement of circulating currents for a case of 240MVA, 220 kV transformer is presented along with a numerical calculation of circulating currents and compared with the measurement.**

***Index Terms*—Power transformer, split-winding, circulating currents.**

I. INTRODUCTION

One of the common multi winding topologies used in power transformers are two low-voltage windings placed one above the other with shared high-voltage winding, known also as split-winding transformers. This kind of transformers are typically used as step-up transformers in power generation systems. With a symmetrical load on both low-voltage windings, split-winding transformers behave entirely like a standard transformer [1]. However, when the load of low-voltage windings is not symmetrical, or in extreme situation, when only one low-voltage winding is loaded, circulating currents will occur in the high-voltage winding. If there is a regulation winding on the high-voltage side, circulating currents will flow also through each regulation winding. Reason for the circulating current occurrence is a magnetic link – a mutual inductance between the windings, and the fact that all the windings on the high-voltage side are electrically connected. Figure 1 shows the principles of circulating current generation. In the case of connection only the upper low-voltage winding, there comes the disbalance of the stray flux. The stray flux of upper low-voltage winding grasps the lower part of the high-voltage winding and induces circulating current in the high-voltage winding loop. This current superposes with the regular current in the upper part of high-voltage winding and appears isolated in the lower part. The same cause of circulating current applies for additional regulation branches in the high-voltage section. In some cases, circulating current can have an opposing direction to the regular current and the regular current of winding is then reduced.

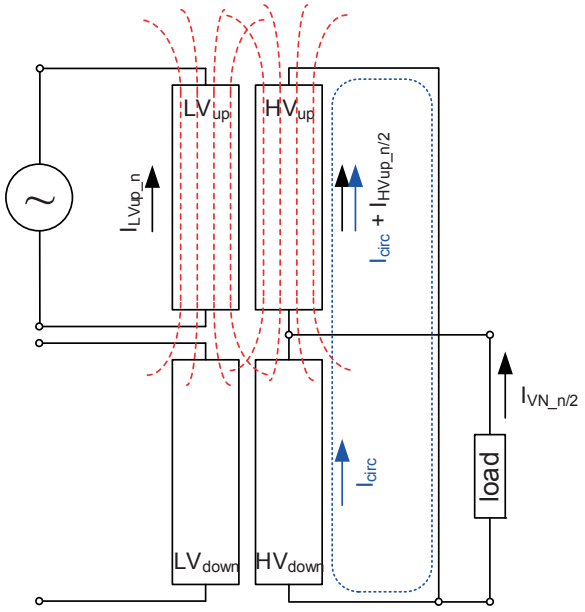

Figure 1: Principle of circulating currents occurrence.

The consequences of circulating currents are increased ohmic and eddy losses in windings, higher stray flux and stray losses amount, changed impedance voltage [2] and higher forces so the transformer has to be designed to withstand higher demands [3][4]. Circulating currents can be avoided in split-winding transformers by using two separate tap changers, the one for upper part and the one for the lower part of regulation winding as this solution would eliminate electrical connection between upper and lower high-voltage and regulating winding, but with a cost of two tap changers. This paper will present detailed measurement of circulating currents for a case of a 240 MVA and 220 kV step-up transformer. Circulating currents are measured in every turn of regulation winding for every tap position as well as in high-voltage winding. Transformer was simulated with FEM model and the calculated results are compared with measurement [5].

II. TRANSFORMER DESCRIPTION

The transformer used for the measurement is a three-phase transformer with three-leg core with nominal power of 240 MVA and nominal voltage 220 kV. It has one regulation winding, reversing type, split on the upper and the lower half. Measurement was conducted with the active part outside of the tank with reduced voltage. This doesn't have an impact on the percentual amount of circulating currents because they depend solely on winding's geometry and winding's mutual inductances.

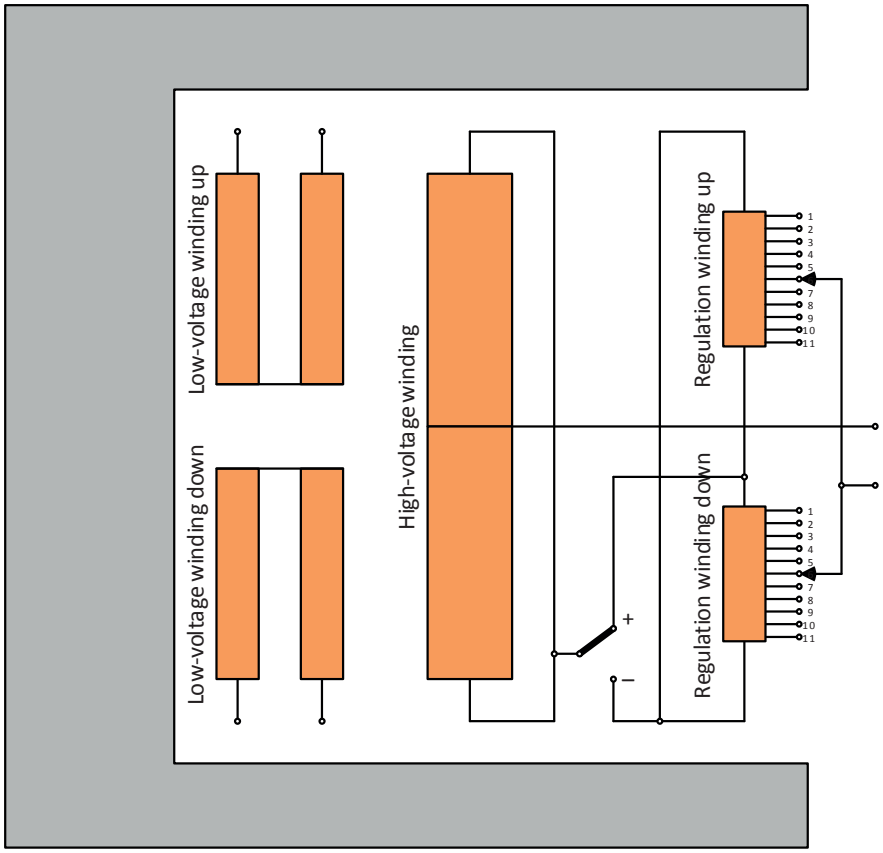

Figure 2: Block scheme of transformer winding and connections.

Every turn of upper part of the regulation winding is connected to the related turn of lower part of regulation winding with a copper bar. Circulating currents are measured on the bars with appropriate equipment.

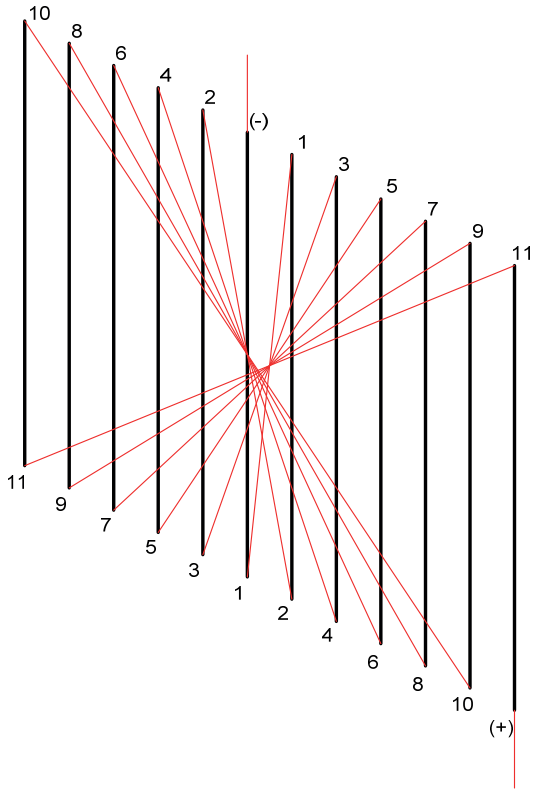

Figure 3: Connections of turns of one part (upper or lower) of regulation winding.

III. MEASUREMENTS DESCRIPTION

The measurement of circulating currents was conducted in the test bay of Končar Power Transformers. Transformer's high-voltage winding was connected to the motor-generator setup. The generator induced 10% of the nominal transformer voltage. Nominal voltage wasn't possible to use because the active part of the transformer was out of tank and oil which is the main insulator and cooling agent and also due to personnel safety. Since circulating currents depend on mutual inductance of windings, current percentage doesn't influence the phenomena. Currents were measured with Fluke true RMS current clamp model 325. For each tap change, voltage was decreased to zero and increased back to 10% of the nominal voltage.

IV. MEASUREMENTS RESULTS

The Table I shows circulating currents in high-voltage winding measured for every tap position. In some cases, circulating current has the same direction as the regular current (positive values) and sometimes has the opposing direction (negative values). An average value of circulating current between upper and lower part of the high-voltage winding is taken as the valid value.

TABLE I. CIRCULATING CURRENTS IN HIGH-VOLTAGE WINDINGS RELATIVE TO THE REGULAR CURRENT.

tap	**1 (+)**	**2 (+)**	**3 (+)**	**4 (+)**	**5 (+)**	**6 (+)**	**7 (+)**	**8 (+)**	**9 (+)**	**10 (+)**	**11 (+)**
HV	100%	100%	100%	100%	100%	100%	100%	100%	100%	100%	100%
HV up	8.8%	8.2%	7.5%	6.8%	6.2%	5.7%	4.8%	4.4%	3.5%	2.9%	2.5%
HV down	9.0%	8.4%	7.5%	7.0%	6.4%	5.9%	5.1%	4.7%	3.8%	3.3%	2.5%
HV average	8.9%	8.3%	7.5%	6.9%	6.3%	5.8%	5.0%	4.5%	3.6%	3.1%	2.5%

tap	12 (K)	13 (0)	14 (-)	15 (-)	16 (-)	17 (-)	18 (-)	19 (-)	20 (-)	21 (-)	22 (-)
HV	100%	100%	100%	100%	100%	100%	100%	100%	100%	100%	100%
HV up	1.8%	1.5%	0.6%	-0.1%	-0.7%	-1.4%	-2.4%	-2.7%	-3.2%	-4.0%	-4.5%
HV down	1.9%	1.2%	0.7%	-0.4%	-0.8%	-1.4%	-2.0%	-2.8%	-3.3%	-4.1%	-4.5%
HV average	1.9%	1.4%	0.7%	-0.3%	-0.8%	-1.4%	-2.2%	-2.7%	-3.2%	-4.1%	-4.5%

The Table II shows the amount of circulating current relative to the regular current for every turn of the regulation winding and for every position of the tap changer. Since the circulating currents have the opposing direction to the regular current, values are negative. In the table there is a separation between the turns of the regulation winding with the regular current (black color) and the turns without the regular current (red color). Even if the tap changer is in such position that regular current cannot flow through the designated turn, that turn is electrically connected with the corresponding turn in the other half of regulation winding and circulating currents can flow in that loop.

TABLE II. CIRCULATING CURRENTS IN THE TURNS OF REGULATION WINDINGS RELATIVE TO THE REGULAR CURRENT FOR DIFFERENT TAP POSITIONS; NUMBERS IN BLACK ARE FOR THE TURNS WITH REGULAR CURRENT, AND NUMBERS IN RED FOR THE TURNS WITHOUT REGULAR CURRENT.

tap ->	1 (+)	2 (+)	3 (+)	4 (+)	5 (+)	6 (+)	7 (+)	8 (+)	9 (+)	10 (+)	11 (+)
T-	-32.9%	-32.3%	-32.2%	-31.8%	-31.1%	-30.8%	-30.3%	-29.9%	-29.8%	-29.3%	-28.9%
T1	-86.4%	-36.2%	-36.3%	-35.4%	-35.5%	-34.5%	-34.1%	-34.0%	-33.5%	-32.7%	-32.5%
T2	-78.9%	-78.7%	-28.2%	-28.2%	-27.8%	-27.4%	-27.2%	-26.7%	-26.3%	-26.1%	-25.7%
T3	-89.9%	-89.4%	-89.4%	-38.7%	-39.0%	-38.0%	-37.3%	-37.4%	-37.0%	-36.4%	-36.1%
T4	-73.7%	-73.8%	-72.9%	-73.2%	-22.2%	-22.3%	-21.9%	-22.1%	-21.3%	-21.5%	-21.1%
T5	-93.2%	-92.9%	-92.7%	-92.2%	-92.2%	-42.1%	-42.1%	-41.3%	-40.9%	-40.1%	-39.8%
T6	-72.4%	-72.1%	-71.8%	-71.8%	-71.0%	-71.7%	-20.5%	-20.9%	-20.0%	-20.3%	-19.7%
T7	-91.6%	-91.8%	-92.1%	-92.0%	-92.0%	-91.9%	-91.7%	-47.2%	-47.0%	-46.0%	-45.8%
T8	-65.6%	-65.7%	-65.3%	-65.1%	-64.9%	-65.2%	-64.6%	-65.3%	-19.1%	-19.4%	-18.6%
T9	-79.7%	-80.2%	-80.6%	-81.0%	-81.3%	-81.7%	-81.9%	-82.3%	-81.9%	-53.1%	-53.3%
T10	-62.2%	-62.0%	-61.6%	-61.9%	-61.3%	-62.1%	-61.3%	-61.6%	-61.1%	-62.8%	-31.2%
T11	-58.8%	-59.4%	-59.6%	-60.1%	-60.5%	-61.3%	-61.5%	-62.1%	-62.3%	-63.1%	-62.5%

tap ->	12 (K)	13 (0)	14 (-)	15 (-)	16 (-)	17 (-)	18 (-)	19 (-)	20 (-)	21 (-)	22 (-)
T-	-28.6%	-22.8%	-23.1%	-23.5%	-23.9%	-24.5%	-24.5%	-24.9%	-25.4%	-25.8%	-26.1%
T1	-31.5%	-31.8%	-19.9%	-19.2%	-20.2%	-20.5%	-20.6%	-21.1%	-21.7%	-22.0%	-22.3%
T2	-25.9%	-25.5%	-25.5%	-26.5%	-26.3%	-26.8%	-26.8%	-27.4%	-27.6%	-28.1%	-28.3%
T3	-35.6%	-35.3%	-34.8%	-35.3%	-16.8%	-16.6%	-16.8%	-17.7%	-18.3%	-18.5%	-19.3%
T4	-21.2%	-20.6%	-20.5%	-19.9%	-20.2%	-31.2%	-30.7%	-31.4%	-31.5%	-31.9%	-32.1%
T5	-39.4%	-39.1%	-38.3%	-38.2%	-37.4%	-37.9%	-13.6%	-13.8%	-15.0%	-15.1%	-15.8%
T6	-19.6%	-19.1%	-19.1%	-18.8%	-18.8%	-17.9%	-18.6%	-33.4%	-33.2%	-34.0%	-33.8%
T7	-45.2%	-44.5%	-43.9%	-43.5%	-42.7%	-42.6%	-41.9%	-42.2%	-9.9%	-9.9%	-11.0%
T8	-18.6%	-18.5%	-18.3%	-17.8%	-17.9%	-17.4%	-17.5%	-16.7%	-17.0%	-36.2%	-35.4%
T9	-52.3%	-51.6%	-50.7%	-50.1%	-49.4%	-48.9%	-48.1%	-48.0%	-47.0%	-47.4%	-5.9%
T10	-30.6%	-30.3%	-29.9%	-28.8%	-28.3%	-28.1%	-28.7%	-27.2%	-26.9%	-26.3%	-27.1%
T11	-59.4%	-59.0%	-58.1%	-57.2%	-56.4%	-56.1%	-55.1%	-54.8%	-53.9%	-53.6%	-52.2%

V. MEASUREMENT ANALYSIS

Figure 4 shows circulating currents in high-voltage winding relative to the regular current. When displayed in a chart, circulating currents shows linear dependence to the tap position. When tap changer deactivates one by one turn of the regulation winding, then comes to (0) position and then activates one by one turn with the opposing polarity, mutual inductance conjunction of high-voltage winding is changing gradually. The chart is not symmetrical regarding percentage of circulating currents because transformer's windings don't have the same distance to the upper and lower yoke due to different insulating distance. This is the cause of different mutual inductance conjunction for terminal tap positions.

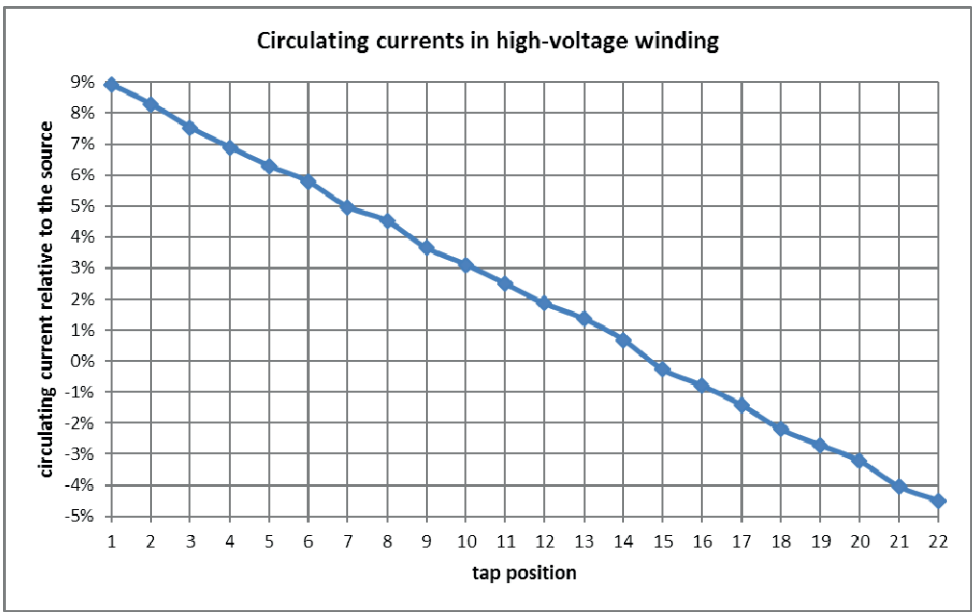

Figure 4: Circulating currents in high-voltage winding relative to the regular current.

Due to different geometry of regulation winding (for every tap position there is always equal number of turns active in the upper and the lower part), circulating current have different dependence to the tap positions. Percentage value of circulating current in individual turn is almost independent to the tap position (Figure 5 and 6). However, the amount of circulating current dramatically differ from turn to turn. For that reason, the Table III and Figure 7 show circulating currents in the turns of regulation windings relative to the regular current; average for all tap positions and grouped in (+) tap positions, no current and (-) tap positions.

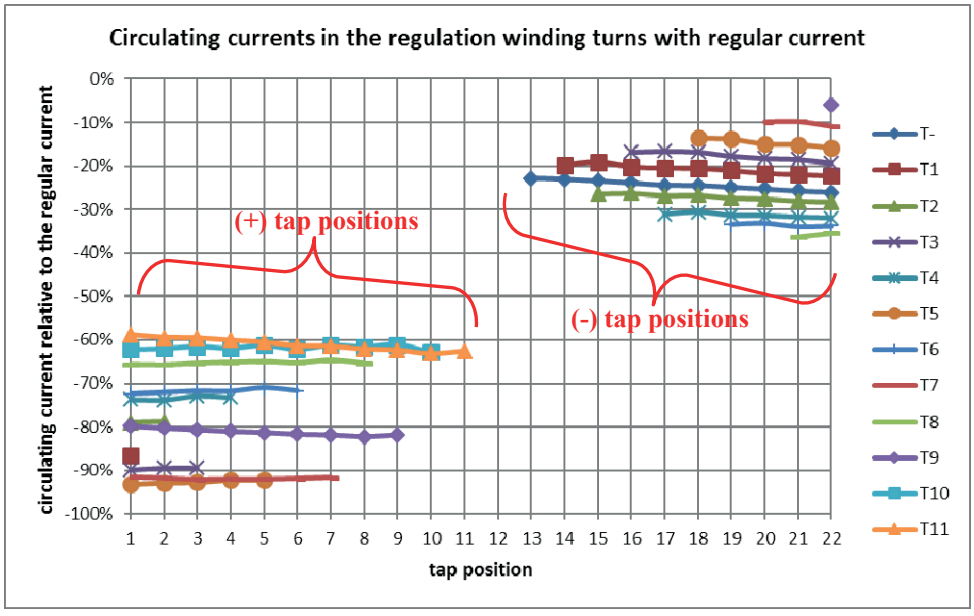

Figure 5: Circulating currents in the turns of the regulation winding with regular current relative to the regular current.

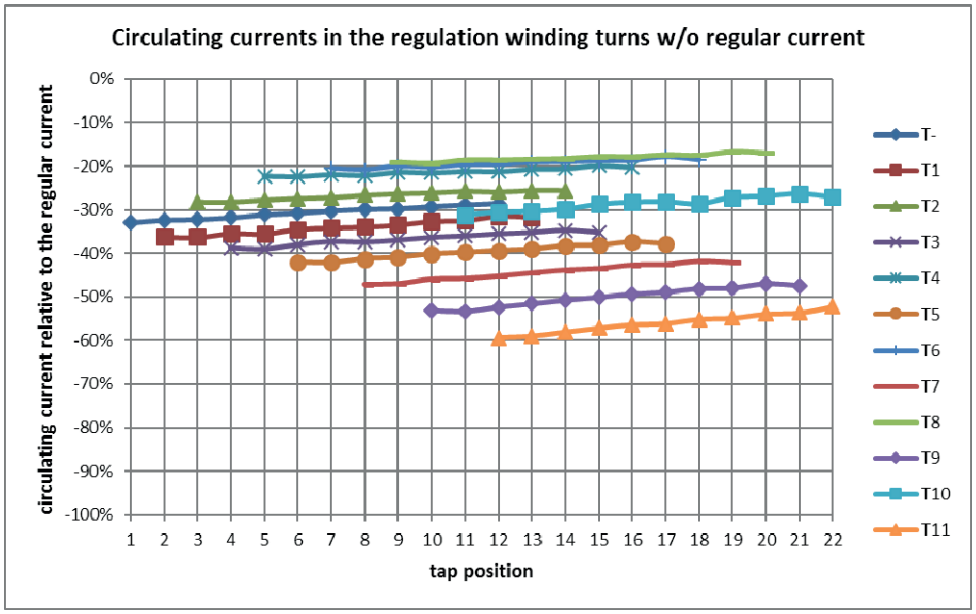

Figure 6: Circulating currents in the turns of the regulation winding without regular current relative to the regular current.

TABLE III. CIRCULATING CURRENTS IN THE TURNS OF REGULATION WINDINGS RELATIVE TO THE REGULAR CURRENT; AVERAGE FOR ALL TAP POSITIONS AND GROUPED IN (+) POSITIONS, NO REGULAR CURRENT AND (-) POSITIONS.

turn	average (+)	no regular current	average (-)
T-		-30.9%	-24.4%
T1	-86.4%	-34.5%	-20.8%
T2	-78.8%	-27.1%	-26.9%
T3	-89.6%	-37.5%	-17.7%
T4	-73.4%	-21.8%	-31.5%
T5	-92.6%	-41.1%	-14.7%
T6	-71.8%	-20.3%	-24.7%
T7	-91.8%	-46.5%	-10.2%
T8	-65.2%	-19.0%	-35.8%
T9	-81.2%	-53.2%	-5.9%
T10	-61.8%	-31.2%	
T11	-61.0%	-56.0%	

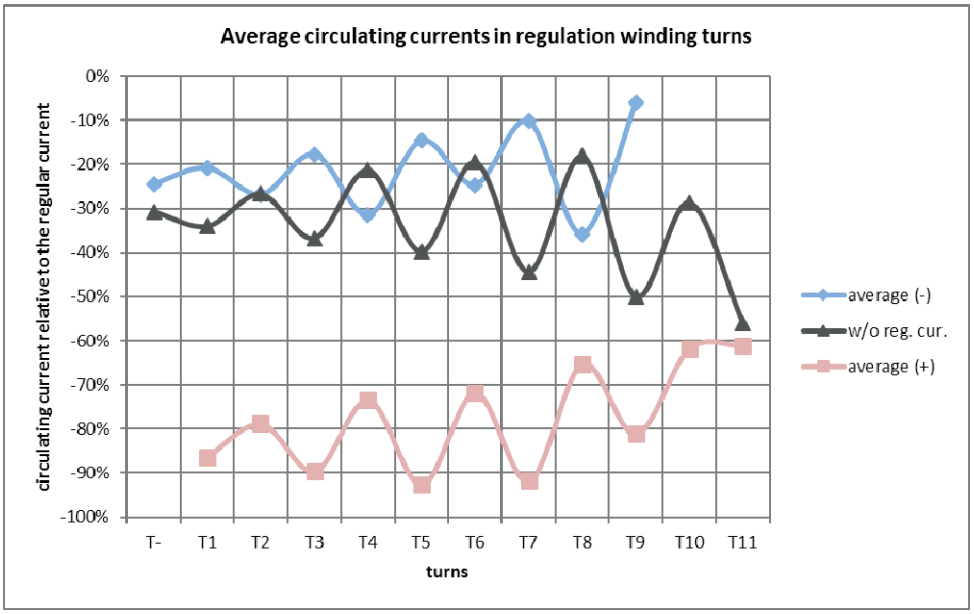

Figure 7: circulating currents in the turns of regulation windings relative to the regular current; average for all tap positions and grouped in (+) positions, no current and (-) positions.

VI. NUMERICAL CALCULATION

For the purpose of showing principles of numerical calculation of circulating currents here is presented 2D FEM model with simplified regulation winding. The model was calculated with Ansys Maxwell in magnetic transient mode. The model is 2D rotational symmetry with linear material properties. Winding blocks electrical connection is defined through associated electrical scheme, which is the integral part of the model. Regulation winding is represented as one block for upper part and one block for lower part of the winding. This approach can give good results for terminal tap positions where all or almost all the turns of the regulation winding carry regular current. For intermediate tap positions each turn and its associated electrical scheme has to be modeled individually.

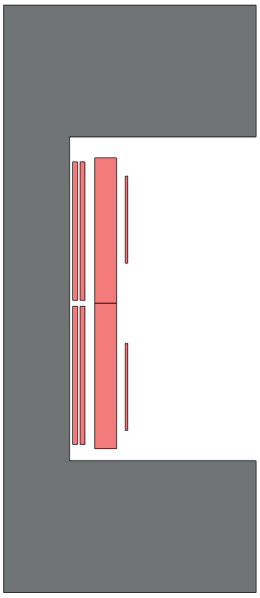

Figure 8: 2D FEM model for circulating current calculation.

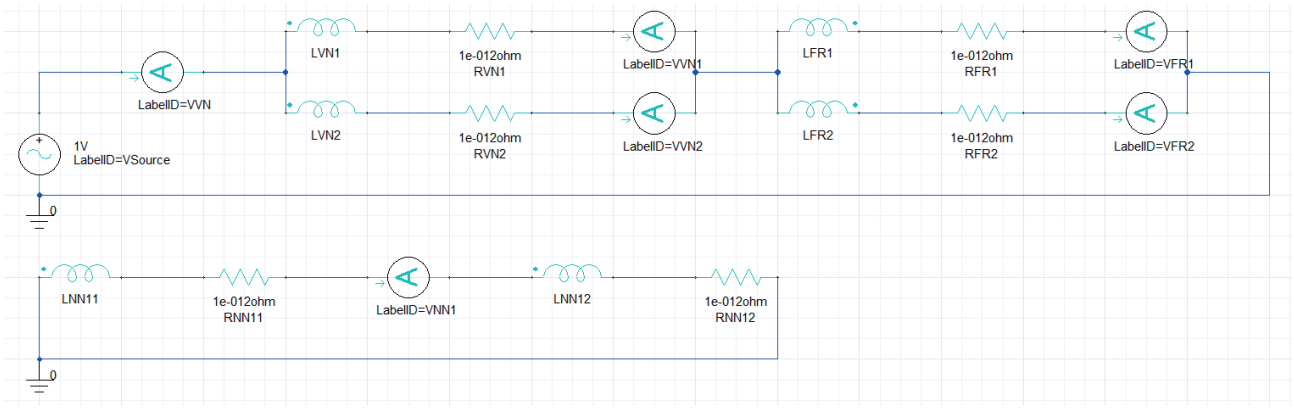

Figure 9: electrical connection of windings in 2D FEM model for circulating current calculation.

TABLE IV. CALCULATED AND MEASURED CIRCULATING CURRENTS IN THE HIGH-VOLTAGE AND REGULATION WINDINGS RELATIVE TO THE REGULAR CURRENT FOR TERMINAL TAP POSITIONS.

tap position	HV calculated	HV measured	regulation w. calculated	regulation w. measured
1 (+)	8.2%	8.9%	-89.0%	-86.4%
22 (-)	-5.1%	-4.5%	-16.4%	-26.1%

For the sake of comparison in the Table IV there are calculated average measured circulating currants for the tap positions 1 ((+) position) and 22 ((-) position). The Table IV shows very good agreement for the tap position 1 and acceptable agreement for the tap position 22.

VII. CONCLUSION

Circulating currents occur in split-winding transformers in the cases of asymmetrical load of upper and lower low-voltage windings. Circulating currents flow in the loops of high-voltage and regulation windings. This paper presents comprehensive measurements of circulating currents on the 240 MVA and 220 kV step-up transformer. Circulating currents are measured in upper and lower part of high-voltage and regulation windings for every tap position and every turn of regulation winding. Measurement analysis shows that for this type of transformer circulating currents in high-voltage winding linearly depend on the tap position. However, for the regulation winding it was shown that circulating currents in winding's turns are practically independent to tap position and can be grouped in three groups: (+) tap positions, no current and (-) tap positions where circulating currents depend solely on the physical location of the turn. Finally, a numerical calculation of circulating currents was presented. Numerical calculation is carried out with 2D FEM model with associated electrical scheme. It is shown that modeling windings as blocks can be used with satisfactory precision for calculation of circulating currents for terminal tap position where all or almost all the turns of the regulation winding carry regular current, while for intermediate tap positions each turn and its associated electrical scheme has to be modeled individually.

VIII. REFERENCES

[1] K.Karsai, D.Kerenyi, and L.Kiss, "Large Power Transformers*," Elsevier, 1987.*

[2] H. Fukumoto, T. Furukawa, H. Itoh, and M. Ohchi, "Calculating leakage reactance of 9-winding transformer using time-dependent 3D FEM analysis," IECON 2015 - 41st Annu. Conf. IEEE Ind. Electron. Soc., pp. 4459–4464, 2015.

[3] Longnv Li, and Xiaoming Liu, "Calculation and Analysis of Short-circuit Performance of a Split-Winding Transformer with Stabilizing Windings*," Proceedings of 2018 IEEE International Conference on ID8062 Applied Superconductivity and Electromagnetic Devices Tianjin, China, April 15-18, 2018.*

[4] G. B. Kumbhar, and S. V. Kulkarni, "Analysis of Short-Circuit Performance of Split-Winding Transformer Using Coupled Field-Circuit Approach*," IEEE Transactions on Power Delivery, Vol. 22, NO. 2, April 2007.*

[5] Bruno Jurišić, Tomislav Župan and Leonardo Štrac, "Calculation of Circulating Current Inside Power Transformers in Non-Symmetrical Configurations", International Symposium on High Voltage Engineering August 2019 Budapest, Hungary

Journal of Energy
VOLUME 68 Number 4 | 2019 | Special Issue
journal homepage: http://journalofenergy.com/

Coupled Electromagnetic-Thermal Model Applicable for Distribution Transformers

Ž. Tašner[1] and B. Ćućić[1]
[1] Končar - Distribution & Special Transformers Inc., Josipa Mokrovića 8, 10090 Zagreb, Croatia
E-mail: zeljko.tasner@koncar-dst.hr

***Abstract*—Distribution transformers, with their specific passive cooling mechanism, are investigated in this research. FEM based approach was used for electromagnetic field distribution and losses calculation, following with the methodology for thermal modelling. Detailed temperature measurements using thermocouples and thermal camera were done on 1600 kVA unit, the results of which are compared against calculated values. The aim of this research is to present a viable approach for adequate thermal modelling of distribution transformers applicable for research and design purposes.**
***Index Terms*— coupled electromagnetic-thermal model, distribution transformers, finite element method, losses calculation.**

I. INTRODUCTION

In order to increase the distribution transformer reliability by making them more robust, in some designs an oil conservator is avoided, and a completely closed tank is used. In such solutions, both oil volumetric change due to its temperature rise and transformer cooling capabilities are resolved using thin cooling fins. Such design imposes a natural oil flow within the transformer and hence careful design practice needs to be taken in order to adequately model the fin number and total cooling area. A number of different approaches exists, ranging from analytical/empirical methods, through static conductive thermal simplifications to detailed models using computational fluid dynamics (CFD) solvers [1]–[4].

Since the heat originates from the overall losses within the transformer, all of the approaches have to be electromagnetically-thermally coupled to some degree; they need to address the loss calculation as a first step, and then obtain the temperature distribution using thermal models [5], [6]. These losses can also be calculated in several ways, depending on the needed accuracy and calculation speed, using either analytical and semi-empirical methods or modern numerical approaches such as finite element method-based (FEM) solvers.

There are two main heat-generating sources within the transformers: the first one are the ohmic losses in current-carrying conductors such as windings and leads, and the second one are additional losses within other metallic parts such as clamping system and transformer tank. The former ones are the main losses and need to be considered when adequately modelling winding oil ducts and transformer cooling system. The latter ones, arising from stray magnetic field within metallic elements, have to be taken into account in order to avoid local temperature hotspots. These can cause either oil, paint or gasket deterioration, depending whether they occur within the transformer or outside on its tank.

This work presents the use of FEM-based approach for both additional losses and thermal calculations, and the results obtained from numerical models will be compared against the measurements on a 1600 kVA distribution unit. In Section II, the overview of the electromagnetic and thermal modelling approach is given. The following section shows the experimental results, obtained using both thermocouple and thermal camera results. Section IV presents the comparison of the results and finally the conclusion of this research is given.

II. FEM-BASED MODEL

A distribution transformer unit rated at 1600 kVA, 22000/420 V, with passive cooling and without oil conservator was used in this research. Loss and thermal calculations were done using Mentor Graphics® MagNet and ThermNet software, respectively. A 3D model is visible in Fig. 1, showing all the parts relevant for loss and thermal calculations modelled. This includes both the low and high voltage windings, iron core, clamping structure, additional supporting elements, low voltage leads and transformer tank with cooling fins. High voltage leads and bushings were not modelled since they carry insignificant amount of current for generating additional losses.

A. Electromagnetic modelling

A non-linear time-harmonic solver with adaptive mesh was used for electromagnetic calculation. The windings and leads were modelled as aluminum, the iron core as electrical steel, and all the other elements as low carbon steel apart from the non-magnetic insert surrounding the low voltage leads which was modelled using stainless steel material. The simulation represents the transformer temperature rise test. Therefore, low voltage windings were shorted, and the currents were set slightly larger than nominal, to account for both short- and open-circuit losses. All the currents correspond to the ones obtained during the temperature rise measurements presented in Section III.

The visualization of the total loss distribution is given in Fig. 2, omitting the irrelevant elements for better visibility of the results. Additional losses are defined as losses in clamping structure, supporting metal elements, transformer tank wall, cover and bottom. Using proprietary factory software, these losses were calculated at 1037.6 W. Presented simulation gives 1062.6 W, which shows the validity of the model used in this research. As can be seen in Fig. 2, the advantage of using detailed FEM-based models is in the possibility of knowing the distribution of these losses which

can help in locating the regions where temperature hotspots can occur. On the other hand, these models, being time-consuming and complex, are not applicable in the design phase of the transformer.

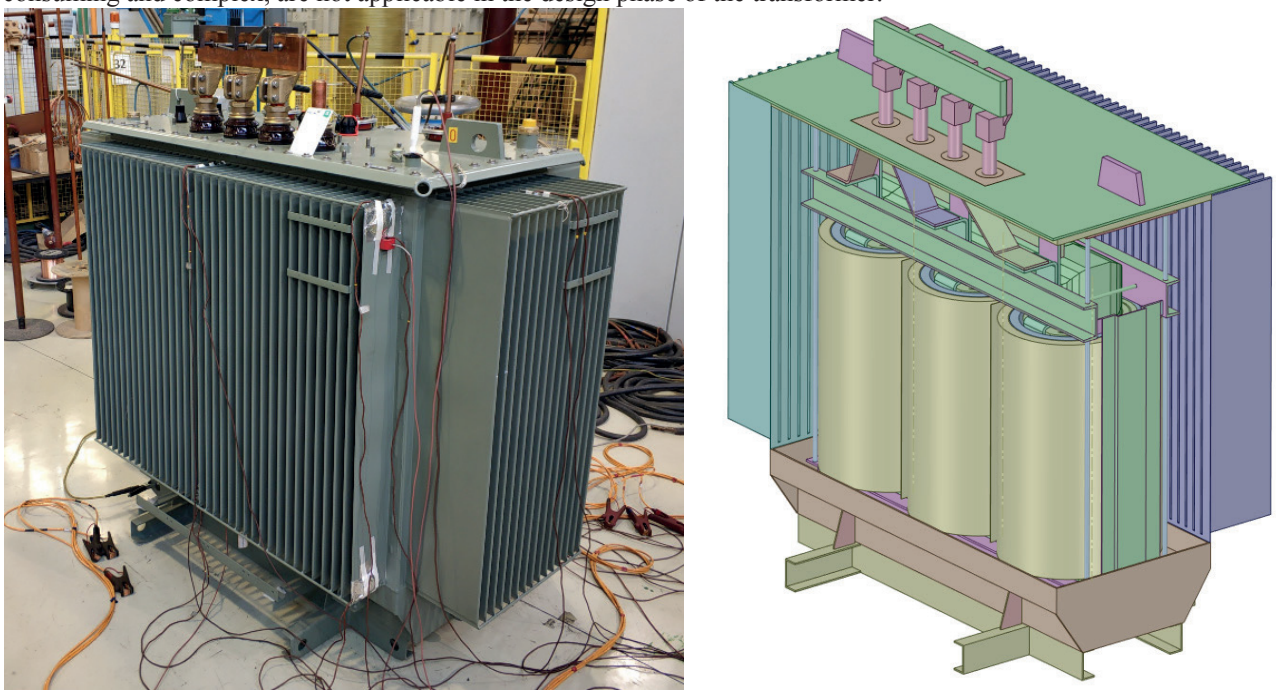

Figure 1: 1600 kVA distribution transformer unit (left) and its 3D model applicable for loss and thermal calculations (right).

B. Thermal modelling

After the electromagnetic calculation was done, it was coupled with thermal solver. Since this work was focused on obtaining the additional losses in metallic parts arising from the stray flux, the increase in oil temperature was calculated using the proprietary factory software . This can be solved using either semi-empirical formulations, thermal network models or CFD solvers, none of which is the scope of this paper.

The cooling of the simulated transformer is only done using natural convection of air [7], [8]. This was modelled as an air boundary with convective heat transfer coefficient of 5 W/(m^2·C). The surrounding air temperature was set to 23.8 °C, so the results can be comparable with the measurements in Section III. The results from the FEM-based solution, shown in Fig. 3., show the computed temperature distribution along the transformer tank and cover. There are no pronounced temperature hotspots and the overall maximum tank temperature is within the expected limits.

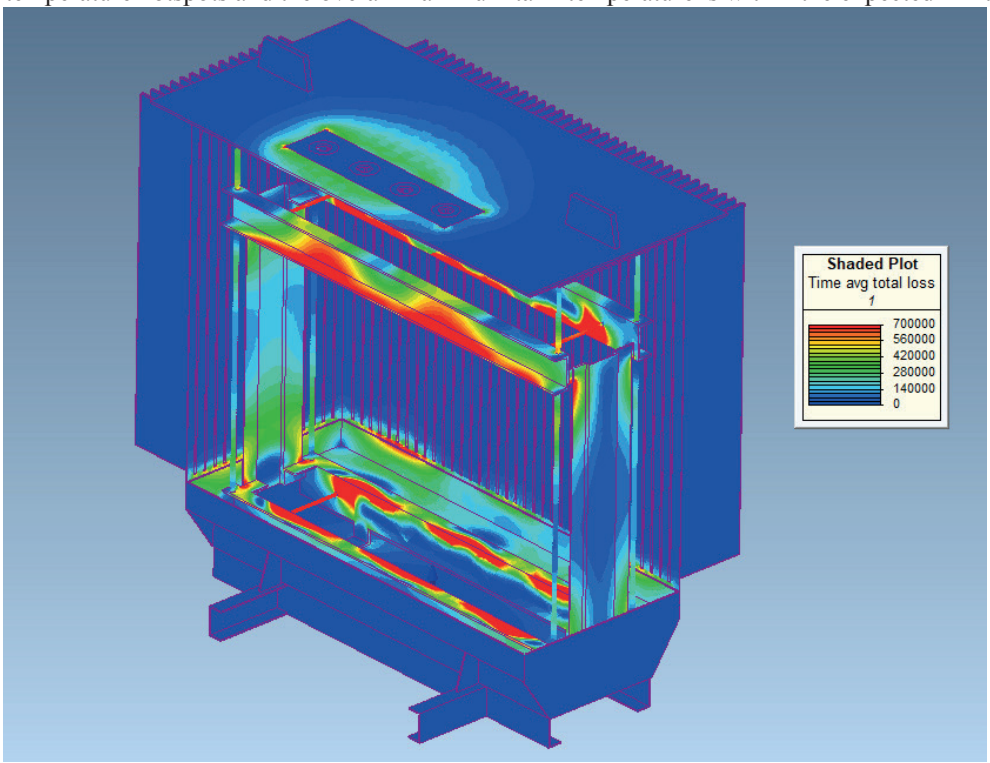

Figure 2: Visualization of the calculated additional losses distribution on relevant elements in the model obtained using Mentor Graphics® MagNet.

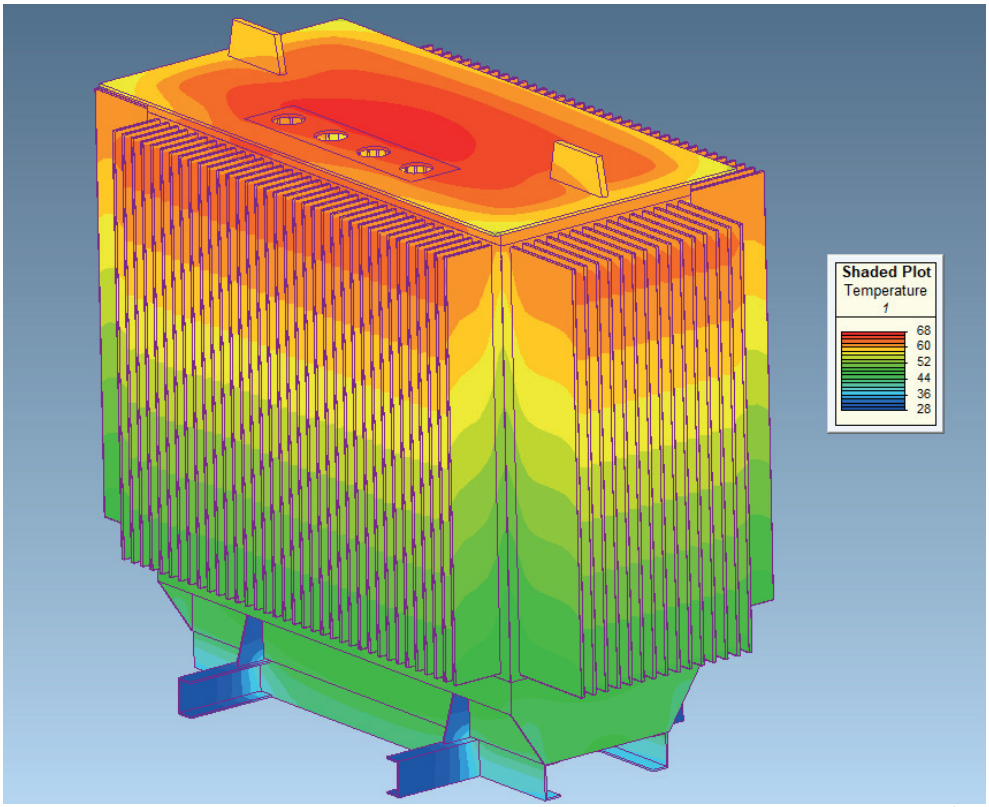

Figure 3: Visualization of the calculated temperature distribution on the transformer tank obtained using Mentor Graphics® ThermNet.

III. TEMPERATURE RISE TEST

The transformer unit under consideration underwent the standard temperature rise test in the factory (see Fig. 1). Since the aim of this research is to evaluate the FEM-based approach to thermal modelling, more detailed thermal measurements were done. Two approaches were used: discrete point measurements from thermocouples on the transformer tank, and overall thermal imaging using a thermal camera.

Two sets of 9 thermocouples were placed on 9 different locations on the tank, visible in Fig. 4. Positions P1-P4 had two sets, one at the bottom and one at the top of the cooling fin. Position P5 had only one set at the top of the fin, due to the lack of additional measuring channels. Each set consisted of two thermocouples: one was only taped to the fin, and the other one was glued using the thermal paste and additionally thermally insulated from the surroundings. This was done in order to measure the relevant temperatures as accurately as possible.

The thermocouple measurements were recorded using Fluke 2635A Hydra Series II in time steps of 15 minutes. The results are given in Fig. 5. Slight lowering of the temperatures during the end of the recording period is due to the end of the temperature rise test and lowering of the current to its nominal value for the winding resistance/temperature measurement. Images from the FLIR thermal camera are visible in Fig.6.

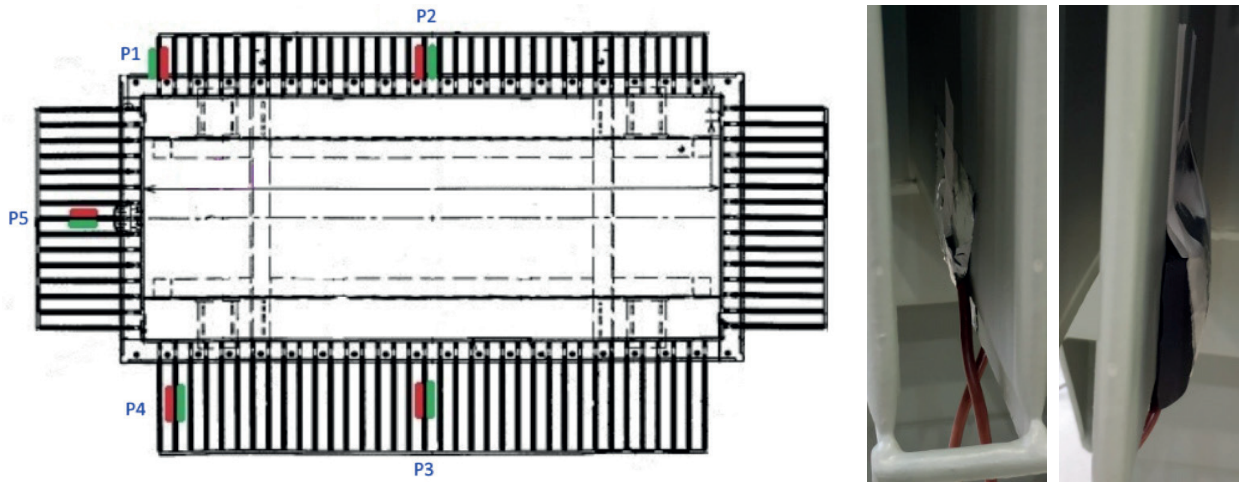

Figure 4: Location of the thermocouples during the temperature rise test (left). At each location, two thermocouples were placed, taped and insulated (right).

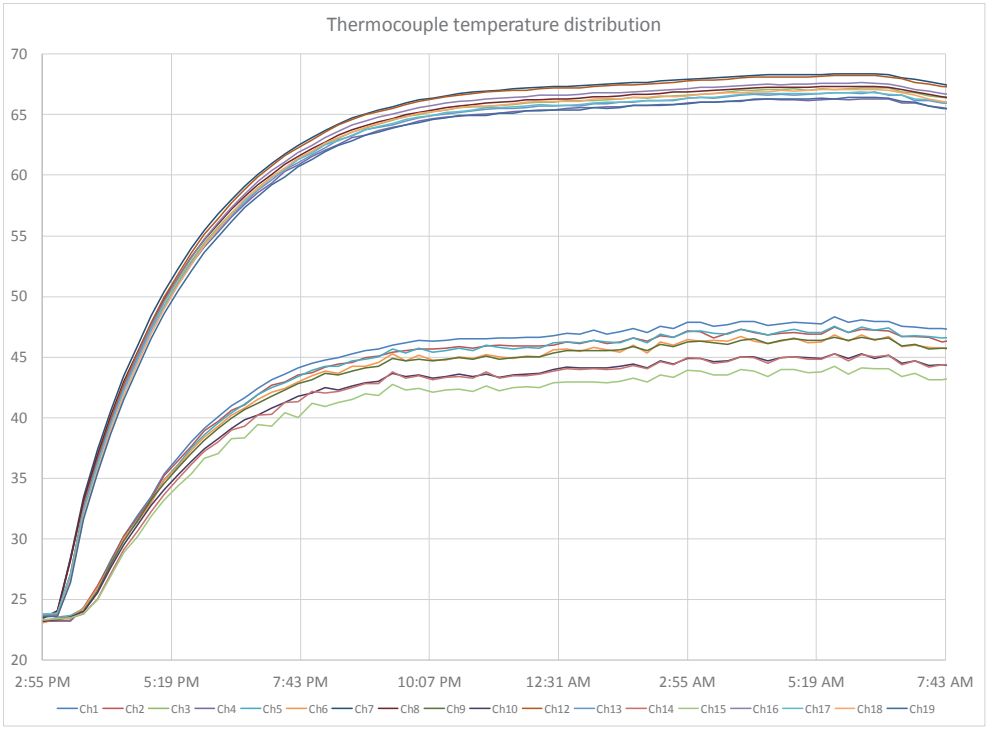

Figure 5: Thermocouple temperature measurements during the test.

The thermal images show the temperature distribution along the transformer tank and its cooling fins. As can be seen, there are no significant temperature hotspots on either the tank cover or the tank sides.

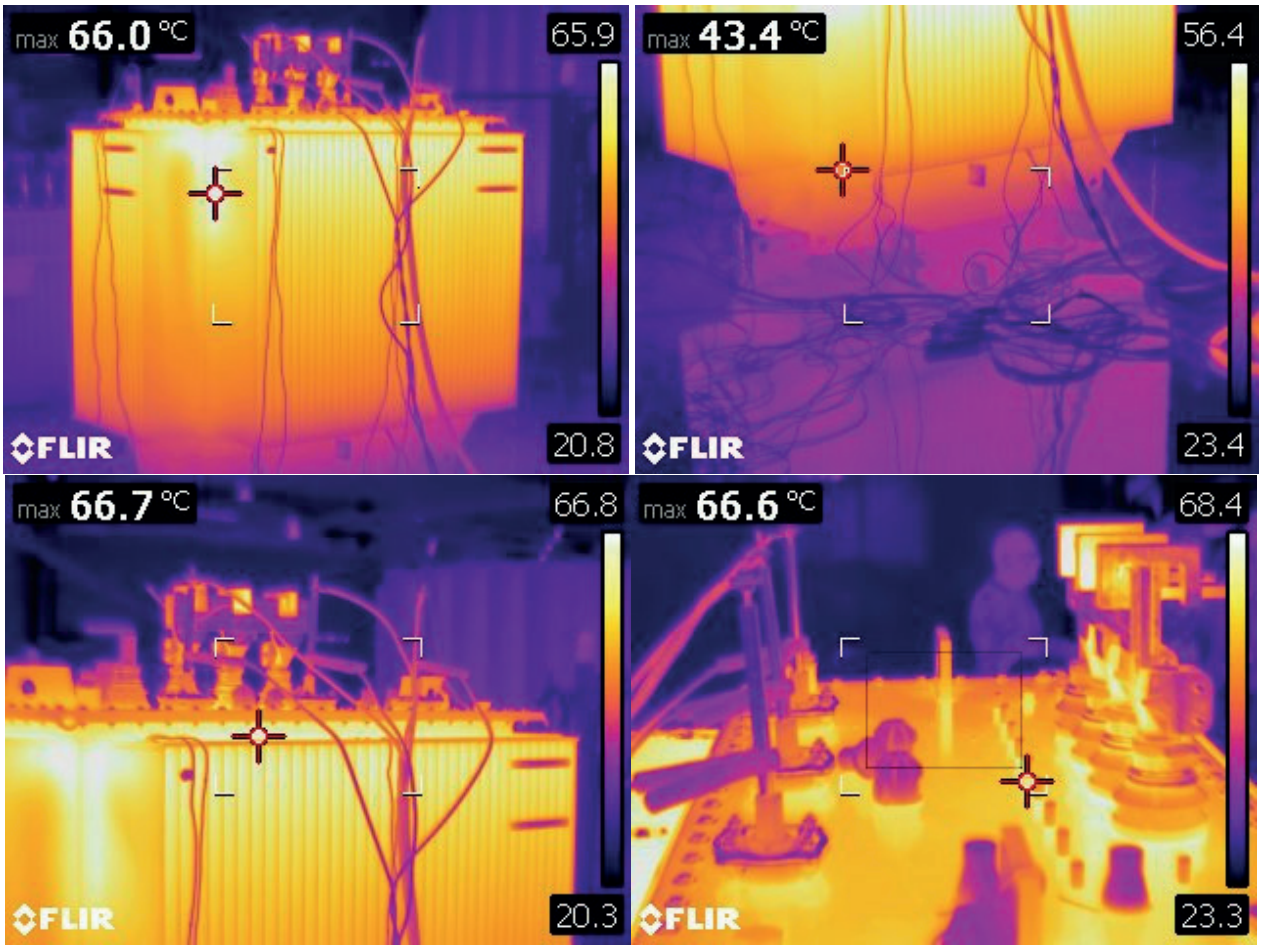

Figure 6: Thermal images obtained using the FLIR thermal camera.

IV. RESULTS

Table I shows the comparison of the thermocouple temperature difference between the two different thermocouple fixation methods on the cooling fin. As can be seen, there is an overall average difference of 1 °C, where glued and insulated readings were always higher.

Qualitatively comparing the images from the thermal camera (Fig. 6) and the temperature distribution visualization obtained using the presented FEM-based approach (Fig. 3), the results are in a good agreement. Table I shows the quantitative comparison of the results at the positions of the thermocouples. In average, there is less than 3 °C difference between measurements and calculations, which is satisfactory. Table II shows quantitive comparison of the calculation results and standard factory heat run test.

TABLE I COMPARISON OF THE TEMPERATURES OBTAINED USING THERMOCOUPLE MEASUREMENTS AND FEM-BASED SIMULATION

	P1 bottom	**P1 top**	**P2 bottom**	**P2 top**	**P3 bottom**	**P3 top**	**P4 bottom**	**P4 top**	**P5 top**
Taped [°C]	47.5	66.3	46.8	67.4	45.3	66.8	44.2	66.8	66.3
Glued + Insulated [°C]	48.3	67.1	47.5	68.4	46.6	68.2	45.3	67.6	67.1
FEM [°C]	48.9	63.2	48.7	64	47.7	63.8	47.5	63.5	63.6
Diff. (Glued-Taped)	0.8 °C	0.8 °C	0.7 °C	1.0 °C	1.4 °C	1.4 °C	1.1 °C	0.8 °C	0.8 °C
Diff. (FEM-Taped)	1.4 °C	-3.1 °C	1.9 °C	-3.4 °C	2.4 °C	-3.0 °C	3.3 °C	-3.3 °C	-2.7 °C

TABLE II COMPARISON OF THE TEMPERATURE RISES OBTAINED FROM TEMPERATURE RISE TEST-SHORT CIRCUIT METHO, SEMIEMPIRICAL CALCULATION AND FEM BASED SIMULATION

	Top oil	**Average oil**	**HV windng**	**LV winding**
Semi-empirical calculation [K]	39,6	31,7	67.4	45.3
Temp. rise test [K]	42,66	32,95	68.4	46.6
FEM [K]	40,1	32,3		
Diff. (SE-TEST)	-3.06 K	-1.25 K	-1.0 K	-1.3 K
Diff. (SE-FEM)	-2.56 K	-0.65 K		

V. CONCLUSION

This paper presented the results of the coupled electromagnetic-thermal model based on FEM solvers. Both the obtained loss and the temperature distribution results are in a good agreement with measurements. Detailed thermal measurements were done, using both thermocouples and thermal camera. Different thermocouple fixation methods were investigated, and the results are comparable.

This work shows the applicability of FEM-based models in electromagnetic and thermal calculations. The presented approach, adapted from model for power transformers, can be useful in the research and development purposes for estimating the temperature hotspots when designing the transformer tank. Limitation of used model are coupled with possibility to simulate heat exchange on both fluid side.

VI. REFERENCES

[1] H. M. R. Campelo, M. A. Quintela, F. Torriano, P. Labbe, and P. Picher, "Numerical thermofluid analysis of a power transformer disc-type winding," in *34th Electrical Insulation Conference, EIC 2016*, 2016, pp. 362–365.

[2] J. Wijaya, W. Guo, T. Czaszejko, D. Martin, N. Lelekakis, and D. Susa, "Temperature distribution in a disc-type transformer winding," in *Proceedings of the 2012 7th IEEE Conference on Industrial Electronics and Applications, ICIEA 2012*, 2012, pp. 838–843.

[3] E. I. Amoiralis, M. A. Tsili, A. G. Kladas, and A. T. Souflaris, "Geometry optimization of power transformer cooling system based on coupled 3D FEM thermal-CFD analysis," in *Digests of the 2010 14th Biennial IEEE Conference on Electromagnetic Field Computation, CEFC 2010.*

[4] J. Cao, H. J. Zhou, and S. X. Qian, "Research on the 3D Temperature Field of Transformer Winding Based on Finite Element Analysis," *Adv. Mater. Res.*, vol. 129–131, pp. 353–357, 2010.

[5] C. Buccella, C. Cecati, and F. de Monte, "A coupled electrothermal model for planar transformer temperature distribution computation," *IEEE Trans. Ind. Electron.*, vol. 55, no. 10, pp. 3583–3590, 2008.

[6] M. A. Tsili, E. I. Amoiralis, A. G. Kladas, and A. T. Souflaris, "Power transformer thermal analysis by using an advanced coupled 3D heat transfer and fluid flow FEM model," *Int. J. Therm. Sci.*, vol. 53, pp. 188–201, 2012.

[7] M.R. Rajkumar, G. Venugopal, S. Anil Lal, "Natural convection from free standing tandem planar heat sources in a vertical channel," in Applied Thermal Engineering 50 (2013) pp. 1386-1395

[8] Jon Gastelurrutia a,*, Juan Carlos Ramos a, Gorka S. Larraona a, Alejandro Rivas a, Josu Izagirre b,Luis del Río , "Numerical modelling of natural convection of oil inside distribution transformers," in Applied Thermal Engineering 31 (2011) pp 493-505)

Journal of Energy

VOLUME 68 Number 4 | 2019 | Special Issue

journal homepage: http://journalofenergy.com/

Determining Natural Resonant Frequencies of Large Power Transformer Windings

Igor Telalović[1], Janko Novosel[1] and Franjo Kelemen[1]
[1]Končar – Power Transformers Ltd., A Joint Venture od Siemens and Končar d.d., J. Mokrovića 12, 10090 Zagreb
Croatia
E-mail: igor.telalovic@siemens.com

Abstract—**Design, assembly process and preparation of windings for large power transformers are complex procedures. It is very important to recognize resonant frequencies of the windings during the design phase in order to avoid increase of vibrations, stresses or noise levels during normal operation of the transformer. Increased vibrations and stresses can occur when the frequency of the excitation is close to the natural resonant frequency of the system. In that case amplitudes will increase, and their values will depend, among other factor, also on the amount of damping present in the system. Therefore, in order to avoid very large amplitude of vibration at resonance, the natural frequency must be known.**
In this work analytical calculation of natural frequencies of high voltage and low voltage windings, is described. Additionally, numerical analysis (FEA) is performed in the software package Ansys. Analysis contains descriptions of geometry simplifications, boundary conditions, mesh validation and applied loads. Finally, results obtained with numerical analysis (FEA) are compared with analytical results.

Index Terms—**Power transformer, natural frequencies, vibrations, finite element analysis**

I. INTRODUCTION

Large power transformer windings are a complex construction comprised of several very different materials. Certain portion of the winding height consists of winding insulation which is, usually, mostly paper and transformerboard. These materials are significantly less stiff than copper, which causes the winding to act in axial direction as a spring, or set of springs, when under stress due to axial forces exerted on the copper conductors.

Axial force per unit of the winding height is usually at its highest value, in absolute form, near the winding ends (bottom and top), with the force near the winding top acting downwards and force near the winding bottom acting upwards. In such cases the accumulated axial force is at its highest value near the middle of the winding. An example of the axial force distribution on the copper conductors and the accumulated axial force along the winding height is given in Figure 1. These forces are periodic, with their base frequency being 100 Hz in 50 Hz network. For this reason, it is important to know the natural resonant frequencies of the transformer windings, in order to be sure that they are not close to excitation frequency or its higher harmonics. In this paper, the object of analysis is to determine the natural resonant frequencies in axial direction of the 500 MVA autotransformer windings using the developed FEM model and analytical model.

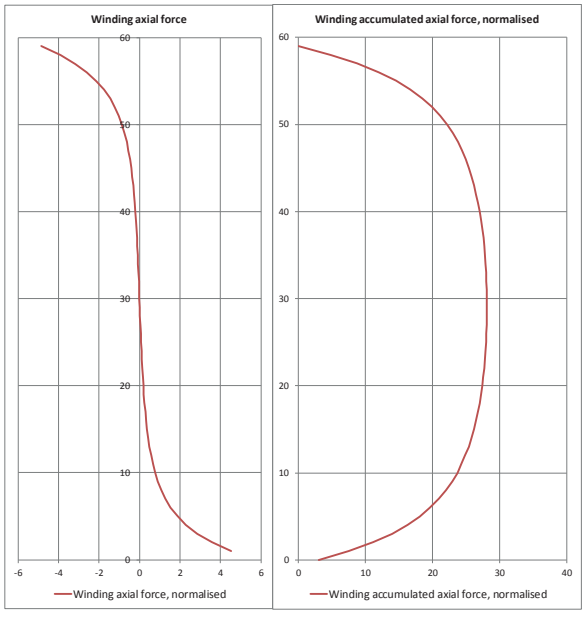

Figure 1 - Example of the winding axial and axial accumulated forces

Igor Telalović, Janko Novosel, Franjo Kelemen, Determining Natural Resonant Frequencies of Large Power Transformer Windings, Journal of Energy, vol. 68 Number 4, Special Issue (2019), p. 21–28

II. GENERAL

In order to calculate the natural resonant frequencies in axial direction an appropriate model has to be developed. The model has to take into account all important features of the winding geometry and the properties of the materials used, without, in the end, being too complex or time-consuming for simulation and calculation.

For the purpose of this calculation, large power transformers windings model will consist of:

- copper conductors (which can be continuously transposed conductors or CTCs)
- paper insulation
- transformerboard spacers (when the winding has radial cooling channels)
- bottom and top support

For simplification purposes, some geometry details of the actual transformer windings will be omitted from the models such as lead entrances, disc crossovers, transpositions etc. For the same reason, the top and bottom supports, will be modeled as springs with the appropriate characteristics, instead of the full-detailed design of supports, which, depending on the whole winding assembly of one limb, could be complex and not necessarily rotationally-symmetric due to all other aspects such as winding leads, oil paths etc.

Two model variations are developed. In the first one, each disc is modeled as a separate element; while in the other variation whole windings are modeled as a homogeneous column with its own set of properties. The model with separate copper parts and insulation parts as well as a homogenous column model are shown in Figure 2

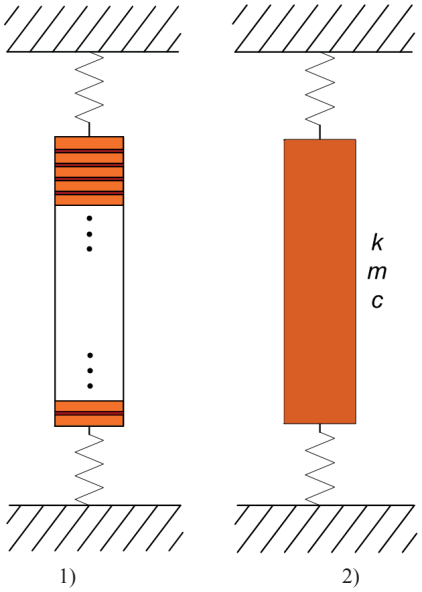

Figure 2 - Model of a transformer winding 1) with copper parts and insulation parts and 2) homogenous column

For the calculation of the natural frequencies, two distinct approaches have been employed.

A. Finite element method approach
for model 1)

B. Analytical approach
for model 2)

The general data of the transformer windings is given in TABLE I.

TABLE I GENERAL DATA OF THE TRANSFORMER WINDINGS

Property	Winding A	Winding B
Number of discs	184	130
Height of copper disc	10,9 mm	12,7
Height of paper insulation	1,12 mm	1,2 mm
Height of transformerboard spacers	N/A	4 mm
Winding nominal height	2220 mm	2286 mm
Winding mass	7435 kg	5052 kg

III. NUMERICAL APPROACH

Numerical simulation, using finite element method, is performed in software package ANSYS 2019. For this type of calculation, where the natural resonant frequencies are in the focus of the analysis, the module "Modal Analysis", available in the Ansys Workbench setup, is used.

CAD models of windings A and B, used for calculation are given in Figure 3

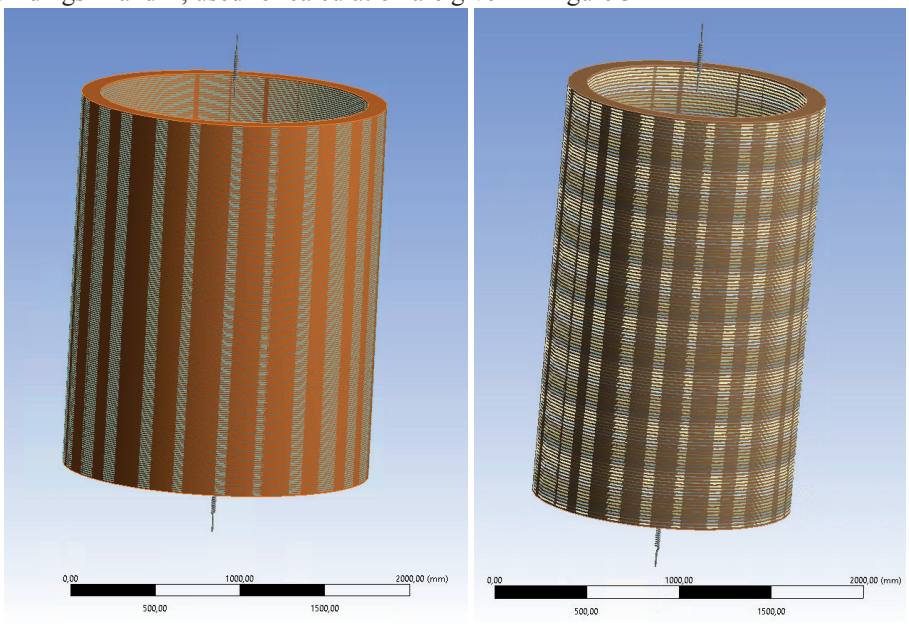

Figure 3: Models of the windings in FEM software

As the focus of this paper are axial natural frequencies, the mesh density in radial direction is of low significance and can be set to 1 mesh element per winding width. However, the mesh density in axial direction is important, and needs to, at the very least, be set at 1 mesh element per winding copper disc and 1 element per insulation between discs. Several cases of calculations were performed, and based on this, in authors' opinion, adequate mesh, which gives appropriate accuracy for the calculation, was chosen.

In case of winding A, the top paper insulation of a copper disc and bottom paper insulation of the disc immediately above can be modeled together as one part, therefore reducing the number of elements along the height of the winding. A detail, showing layers of copper discs and layer of insulation, of the model is given in Figure 4.

Figure 4 - Layers of copper (brown) and paper insulation (grey) during meshing process

For the winding B, which has transformerboard spacers, the exact sequence would be "copper – paper – spacer – paper – copper disc". However, without compromising calculation procedure, this can be modeled as "copper – double paper – spacer – copper". For any winding with spacers, the actual number of spacers can easily reach several thousands, eg. 151 discs with 60 spacers between any two discs would give 9000 spacers. In order to avoid modelling each of the 9000 spacers, the simplification is introduced and all 60 spacer along the winding circumference are modeled as a single disc (as shown in Figure 5) with equivalent parameters, most importantly, the Young's modulus of elasticity of such a disc is altered, due to the fact that now spacer covered surface is significantly larger.

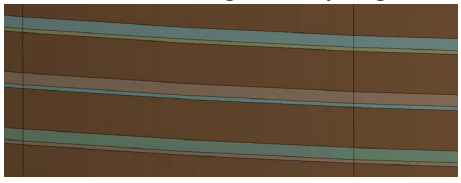

Figure 5 – Layers of copper discs (brown), paper insulation and spacer layer during meshing process

As stated in previous chapter, top and bottom winding support has been modeled using springs that are set between the bottommost disc and ground, as well as, between topmost disc and ground. In order to determine the necessary characteristics of the equivalent spring, several important factors have to be taken into account, notably the construction of the winding top and bottom support including the total surface that can adequately transfer the axial force, the properties of the materials used for their production and relative proportion in the total height of the winding support. Although in the real transformer, depending on the other aspects of design, such as dielectric requests, the height of the top and bottom support, which will affect the equivalent spring characteristic, isn't necessarily the same, for the purpose of the current work the characteristics of the top and bottom spring will be taken to be equal, with values as shown in Table II.

TABLE II EQUIVALENT SPRING CONSTANTS OF THE TOP AND BOTTOM WINDING SUPPORT

No.	Winding A	Winding B
TOP support	6,1 10^5 N/mm	5,0 10^5 N/mm
BOTTOM support	6,1 10^5 N/mm	5,0 10^5 N/mm

The ideal model for such a spring behavior would actually be non-linear, at least in the fact that no tensile force can be transmitted through such a spring. However, compression-only spring is a non-linear element, so it cannot be modeled as such in the Modal analysis. However, with assumption that no separation of elements occurs under appropriate prestress (which holds true for all practical purposes), the modeled spring can be accepted during this calculation procedure.

The results obtained through the numerical simulation, using finite element method in Ansys 19 are given in Table III and Figure 6 (winding A) and Figure 7 (winding B).

TABLE III NATURAL RESONANT FREQUENCIES WINDING A AND B – NUMERICAL APPROACH

No.	Winding A	Winding B
1	56,7 Hz	52,8 Hz
2	137,0 Hz	110,7 Hz
3	236,1 Hz	174,5 Hz
4	340,2 Hz	242,2 Hz
5	446,7 Hz	312,2 Hz

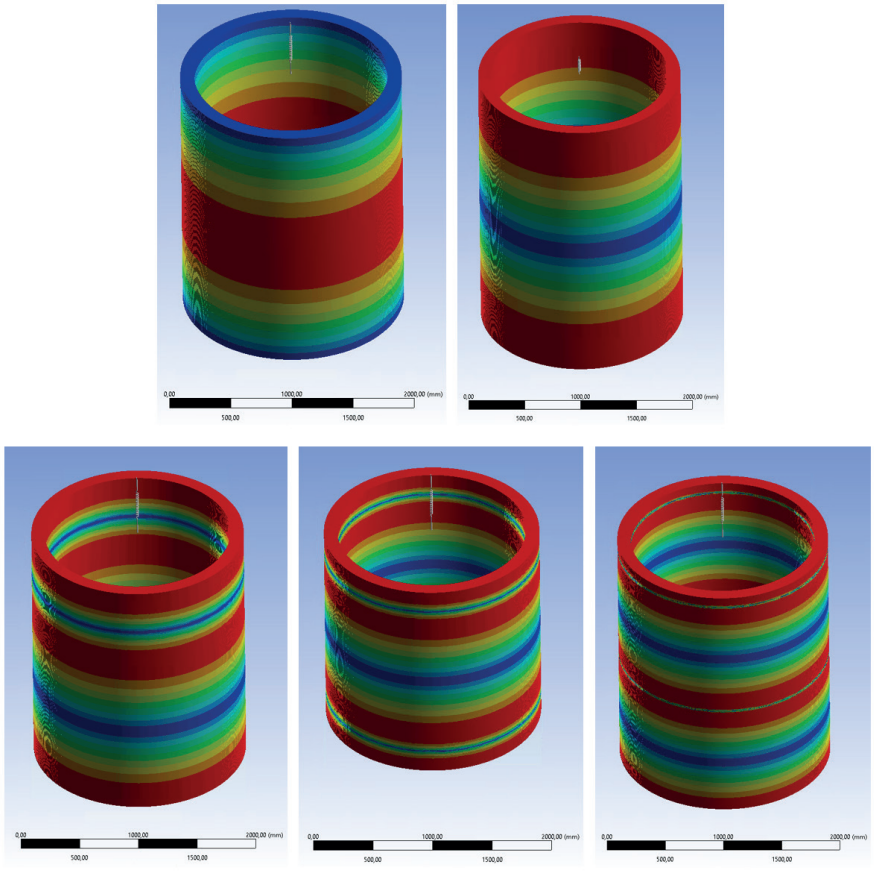

Figure 6 - First, second, third, fourth and fifth mode of axial vibration of winding A

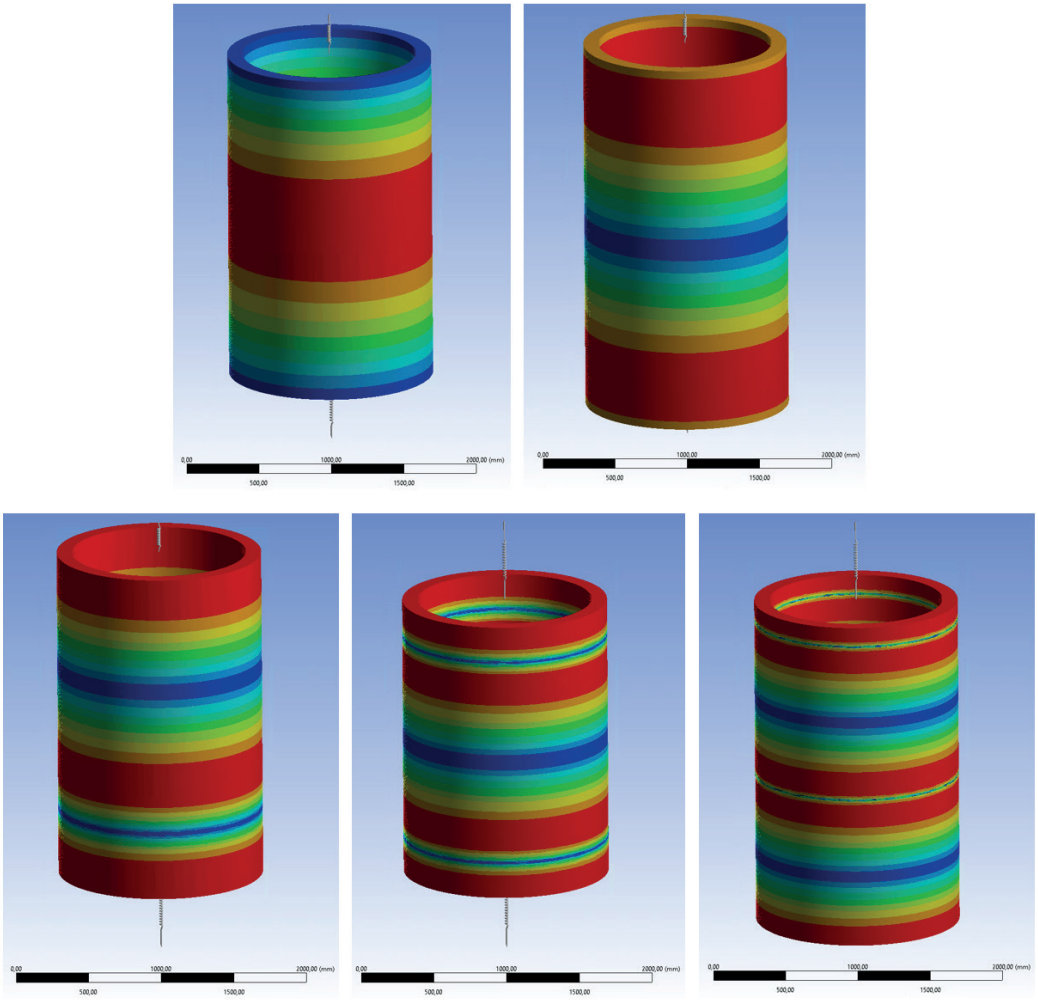

Figure 7 - First, second, third, fourth and fifth mode of axial vibration of winding B

IV. ANALYTICAL APPROACH

As in the case of numerical analysis, similar simplification to the real winding geometry has to be done, in order to derive the differential equation governing the longitudinal dynamic behavior of the winding. The basic schematic for the derivation is given in Figure 8. The winding in this approach is modeled as a homogenous column with its own specific properties, such as mass and stiffness. As several parts of the analytical approach to the task of calculating the winding natural frequencies are explained in [1], detailed step-by-step procedure can here be omitted.

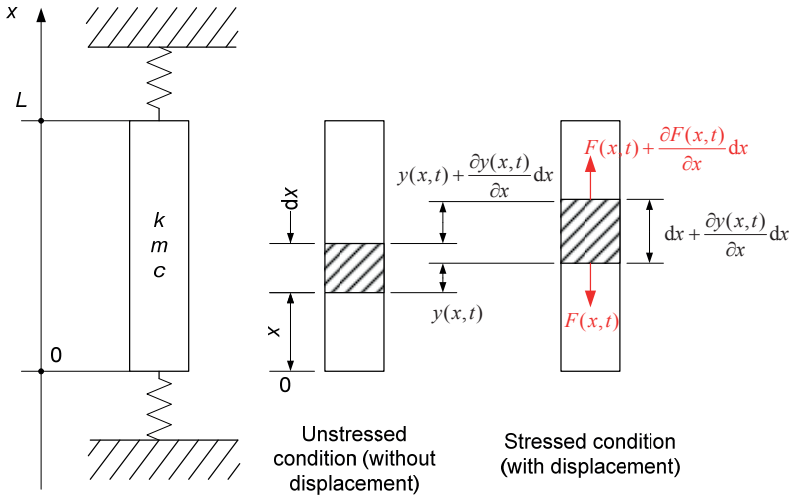

Figure 8 - Basic schematic of a winding and insulation elastic system

The displacement of the differential infinitesimal element of the winding is a function of the coordinate x. If $y(x,t)$ denotes the displacement of the point x in the winding from the rest position, in a strained condition, the element of the length dx changes its length by $(\partial y/\partial x)dx$ and gets strained by $(\partial y/\partial x)$. Due to the elastic properties of the winding, the restoring force F_{el} arises:

$$F_{el} = k\frac{\partial y}{\partial x} \tag{1}$$

Let the mass, the spring constant and damping per unit length of the winding be denoted by m, k, c, respectively. The applied force generated per unit length is:

$$P_0(x,t) = P_1(x)G(t) \tag{2}$$

The Newton's law of motion can be applied to the winding element and (3) follows:

$$\begin{aligned} m\cdot \mathrm{d}x\cdot\frac{\partial^2 y}{\partial t^2} &= (F(x,t)+\frac{\partial F(x,t)}{\partial x}dx - F(x,t)) - c\cdot \mathrm{d}x\cdot v + f(x,t)\cdot \mathrm{d}x \\ m\cdot \mathrm{d}x\cdot\frac{\partial^2 y}{\partial t^2} &= k\cdot\frac{\partial^2 y}{\partial x^2}\mathrm{d}x - c\cdot \mathrm{d}x\cdot\frac{\partial y}{\partial t} + f(x,t)\cdot \mathrm{d}x \\ m\cdot\frac{\partial^2 y}{\partial t^2} &+ c\cdot\frac{\partial y}{\partial t} - k\cdot\frac{\partial^2 y}{\partial x^2} = f(x,t) \end{aligned} \tag{3}$$

This is an inhomogeneous partial differential equation of the second order. To complete the problem definition, the initial and boundary conditions must be applied. The boundary conditions consist of the forces applied to the winding ends:

$$\begin{aligned} K_1 y(0,t) - k\frac{\partial y(0,t)}{\partial x} &= 0 \\ K_2 y(L,t) + k\frac{\partial y(L,t)}{\partial x} &= 0 \end{aligned} \tag{4}$$

Initial conditions are:

$$\begin{aligned} y(x,0) &= 0 \\ \frac{\partial y(x,0)}{\partial t} &= 0 \end{aligned} \tag{5}$$

Using the method of separation of variables, the solution to the equation can be sought as a product of the spatial function that depends only on the x coordinate and the time varying part. Therefore, it can be assumed that the solution is of the form:

$$\begin{aligned} y(x,t) &= S(x)\cdot T(t) \\ \frac{\partial y}{\partial x} &= \frac{\partial}{\partial x}(S(x)\cdot T(t)) = T(t)\frac{\partial}{\partial x}S(x) + S(x)\frac{\partial}{\partial x}T(t) = T(t)\frac{\partial}{\partial x}S(x) = TS' \\ \frac{\partial^2 y}{\partial x^2} &= TS'' \\ \frac{\partial y}{\partial t} &= T'S \\ \frac{\partial^2 y}{\partial t^2} &= T''S \end{aligned} \tag{6}$$

Plugging the derivatives (6) into the original equation leads to:

$$mT''S + cT'S - kTS'' = f(x,t)\,. \tag{7}$$

First, the homogeneous equation is observed:

$$mT''S + cT'S - kTS'' = 0\,. \tag{8}$$

Rearranging and dividing through by kTS gives:

$$\begin{aligned} mT''S + cT'S &= kTS'' \\ \frac{m}{k}\frac{T''}{T} + \frac{c}{k}\frac{T'}{T} &= \frac{S''}{S} \end{aligned}\,. \tag{9}$$

On the left-hand side are functions of time, and on the right-hand side is a function of spatial coordinate. Therefore, for the equation (9) to hold, both sides must be constants. The constant can be chosen arbitrarily. It is convenient to choose

$$\frac{S''}{S} = k = -\mu^2 \tag{10}$$

Now, the spatial differential equation, part of the Sturm-Liouville system as explained in [1], allows us to find eigenvalues of the differential equation with boundary conditions

$$\begin{aligned} &S''+\mu^2 S = 0 \\ &K_1 S(0) - kS'(0) = 0 \\ &K_2 S(L) + kS'(L) = 0 \end{aligned} \quad . \tag{11}$$

First, the homogeneous ODE is solved to obtain

$$S(x) = A\cos(\mu x) + B\sin(\mu x)\,. \tag{12}$$

Now, the boundary conditions are rewritten

$$\begin{aligned} &K_1 S(0) - kS'(0) = 0 \\ &K_2 S(L) + kS'(L) = 0 \\ &S(0) = A \\ &S(L) = A\cos(\mu L) + B\sin(\mu L) \\ &S'(0) = \mu B \\ &S'(L) = -\mu A\sin(\mu L) + \mu B\cos(\mu L) \end{aligned} \quad . \tag{13}$$

Further, for nontrivial solution A and B are not identically zero and

$$\begin{aligned} &K_1 A - k\mu B = 0 \\ &B = \frac{K_1 A}{k\mu} \\ &K_2(A\cos(\mu L) + \frac{K_1 A}{k\mu}\sin(\mu L)) + k(-\mu A\sin(\mu L) + \mu\frac{K_1 A}{k\mu}\cos(\mu L)) = 0 \\ &K_2 A\cos(\mu L) + k\mu\frac{K_1 A}{k\mu}\cos(\mu L) + K_2\frac{K_1 A}{k\mu}\sin(\mu L) - k\mu A\sin(\mu L) = 0 \\ &(K_2 + K_1)A\cos(\mu L) + (\frac{K_1 K_2}{k\mu} - k\mu)A\sin(\mu L) = 0 \\ &K_2 + K_1 + (\frac{K_1 K_2}{k\mu} - k\mu)\tan(\mu L) \\ &\tan(\mu L) = \frac{K_1 + K_2}{k\mu - \frac{K_1 K_2}{k\mu}} \end{aligned} \tag{14}$$

holds. Finally, after some rearranging and substitutions the equation is as in [1]:

$$\begin{aligned} &\mu L \Leftrightarrow \lambda, \bar{K}_1 = K_1 / K_0, \bar{K}_2 = K_2 / K_0, k = K_0 L \\ &\tan(\mu L) = \frac{(K_1 + K_2)K_0 L\mu}{(K_0 L)^2\mu^2 - K_1 K_2} \\ &\tan(\lambda) = \frac{(K_1 + K_2)K_0\lambda}{K_0^2\lambda^2 - K_1 K_2} \\ &\tan(\lambda) = \frac{(\bar{K}_1 + \bar{K}_2)\lambda}{\lambda^2 - \bar{K}_1\bar{K}_2} \end{aligned} \quad . \tag{15}$$

The solution to the spatial part of the differential equation is used in solving the time function part. However, solving the time equation can be avoided in this analysis and the circular frequency of the undamped harmonic oscillation can be written immediately as

$$\omega_n = \lambda_n\sqrt{\frac{K_0}{M_0}}; M_0 = mL\,. \tag{16}$$

The oscillations of the winding are damped, but the damping coefficient is low and so, due to the (17), (16) can be used to calculate the circular frequencies.

$$\omega_{r,n} = \omega_n \sqrt{1-\varsigma^2} \approx \omega_n \tag{17}$$

The natural frequencies are:

$$f_n = \frac{\omega_n}{2\pi} = \frac{1}{2\pi} \lambda_n \sqrt{\frac{K_0}{M_0}} \,. \tag{18}$$

The spring constant of the winding insulation can be calculated using Hooke's law

$$K_0 = \frac{E'_d \, S_{ins}}{H_{ins}} \,, \tag{19}$$

where E'_d is an equivalent dynamic Young's modulus of elasticity, S_{ins} is a cross section area of the insulation perpendicular to the vibration direction, and H_{ins} is the height of the insulation in the winding.
The equivalent dynamic Young's modulus of elasticity depends on several factors, such as the relative content of different materials in the insulation column and for the purpose of this calculation is set at $123{,}8 \cdot 10^8$ Pa for winding A and $165{,}8 \cdot 10^8$ Pa for winding B.

The calculated values for the first five natural frequencies using numerical and analytical approach, are given in Table IV.

TABLE IV COMPARISON OF ANALYTICAL AND NUMERICAL RESULTS

No.	**Winding A**		**Winding B**	
No.	**Numerical result**	**Analytical result**	**Numerical result**	**Analytical result**
1	56,7 Hz	56,4 Hz	52,8 Hz	52,4 Hz
2	137,0 Hz	136,0 Hz	110,7 Hz	110,0 Hz
3	236,1 Hz	232,0 Hz	174,5 Hz	173,6 Hz
4	340,2 Hz	334,1 Hz	242,2 Hz	241,0 Hz
5	446,7 Hz	438,4 Hz	312,2 Hz	310,8 Hz

V. CONCLUSION

Determining the natural resonant frequencies of transformer windings is an important task in evaluating the short-circuit withstand capability of large power transformer. Special attention must be given to this phenomenon during the design and production of large power transformer, in order to ensure that the final product is not affected by it. Otherwise, if such analysis is performed incorrectly or with wrong parameters, the electromagnetic forces may incur overstresses to the transformer windings which can in turn result in the transformer failure.

In this paper two different approaches have been employed in order to determine the natural resonant frequencies of large 500 MVA autotransformer windings. The numerical calculation, using FEM software package ANSYS 2019 and its dedicated module for modal analysis, was performed on the CAD models where over 100 winding discs have been modeled. In the analytical approach the winding was represented by a homogeneous column with equivalent parameters.

The results, for both windings which are of different types, showed that the analytically calculated values of natural frequencies correspond well with the values obtained through the numerical calculation on the developed and more detailed FEM model, which points to the conclusion that analytical calculation is adequate for determination of the windings' natural frequencies, under the condition that the equivalent parameters for both the winding insulation and the top and bottom support are correctly taken into account. In order to take all aspect of winding construction correctly into account when dimensioning transformer windings, one must rely on previous vast experience and gained knowledge.

The dimensioning of large power transformer windings is a very complex procedure which, besides expert knowledge, must be based on extensive successful experience in the design, construction and production of large power transformers and all the design rules and "know-how"-s that come with it.

VI. REFERENCES

[1] Mukund R. Patel, "Dynamic Response of Power Transformers Under Axial Short Circuit Forces", *IEEE Transactions on Power Apparatus and Systems*, Vol. 92, Issue 5, 1973, pp. 1558-1576

[2] William W. Seto. B.S. in M.E., M.S., *Theory and Problems of Mechanical Vibrations*, McGraw-Hill, 1964

[3] Rajko Grubišić, *Teorija Konstrukcija - Primjeri dinamičke analize elemenata konstrukcije*, University of Zagreb, Faculty of Mechanical Engineering and Naval Architecture, 2002.

[4] Ansys documentation and user manual – Release 19.1

Journal of Energy

VOLUME 68 Number 4 | 2019 | Special Issue

journal homepage: http://journalofenergy.com/

The magnetic flux density distribution in the anisotropic transformer core

J. Wojtkun [1], B. Bródka [1] and D. Stachowiak[2]
[1]Power Engineering Transformatory Sp. z o.o., Poznań, Poland
[2]Poznan University of Technology Faculty of Electrical Engineering, Poznań, Poland
E-mail: j.wojtkun@petransformatory.pl

Abstract **The paper discusses the magnetic flux density distribution in medium power transformers core. Three-phase transformers are usually made of grain-oriented electrical steel characterized by anisotropy. Core losses, among other things, mainly depend on the grade of material. The selected results of calculation and measurement of no-load losses of medium power transformers have been shown.**

***Index Terms*— Three-phase transformer, Finite element method, Anisotropy.**

I. INTRODUCTION

An important issue in the design of the distribution transformer is the estimation of the no-load losses. Incorrect estimation of core losses during the design process can result in a financial penalty for the transformer manufacturer. The no-load losses are mainly influenced by the magnetic flux density, the excitation frequency, the mass and the grade of steel as well as other factors [1, 2, 3].

The transformer core is the element guiding the flux and is commonly constructed of rolled grain oriented (GO) electrical steel characterized by anisotropy. That means their magnetic properties differ depending on the examined direction [4, 5, 6]. In rolled material like GO steel, one reference axis corresponds to rolling direction (RD), one axis to lateral or transverse direction (TD), and the third axis is in the normal direction (ND).

This coordinate system for a rolled material is presented in Figure 1. The idea of orienting grains in a magnetically preferred direction was discovered by N. P. Goss. The corresponding texture (110), <001> is called the Goss texture, otherwise known as Cube-on-Edge (COE) see Fig. 1 a. The (110) plane lies in the sheet plane, and the [001] direction points approximately parallel to the rolling direction of the steel. The Goss texture has its highest magnetic permeability and a lower loss when magnetised in the rolling direction than that of other directions. Due to this texture, high values of the flux density can be obtained in the direction of rolling.

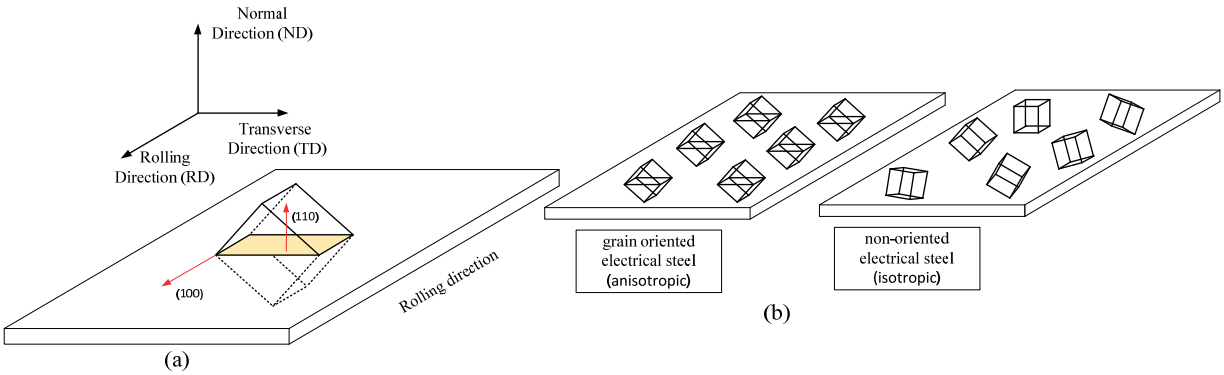

Figure 1. Reference coordinate system for a rolled material and crystal orientation relative to the rolled sheet reference axes for Goss (110)[001] cube-on-edge texture (a); grain-oriented and non-oriented electrical steel (b)

GO steel causes low core losses at high flux density levels when used as a core material in projects with a flux path parallel to the rolling direction, as in transformers. The direction of magnetic flux is consistent with the direction of rolling the sheet in a significant part (yokes and limbs). However, these directions don't overlap in the joints of the yokes and the limbs, as that is the region where the magnetic flux turns and changes the direction. At the corners of the transformer cores, the flux density is not parallel to the rolling direction. The flux in the corner flows from one lamination to another and also changes direction in space. The flux may lean towards to deflect away from the rolling direction of the lamination in the corner area. Owing to the presence of anisotropy in the material, the power losses will increase as the flux deflects from the rolling direction in the lamination plane.

Generally, the main labour in transformer modeling is concentrated especially on modeling the nonlinearities and the anisotropy of the core [8, 10, 14]. This paper deals with the modelling and analysis of a three-phase core-type transformer. The magnetic flux density distribution has been considered as well as the calculation and measurement of no-load losses of medium power transformers.

II. THE CALCULATION AND MEASUREMENTS OF NO-LOAD LOSSES

On the whole, core losses (no-load losses) estimation methods in transformers can be classified into four main categories: measurement (empirical) methods [1,2,7,8], equivalent circuit methods [8,9,10], artificial intelligence methods [8,11,12] and numerical methods [8,13,14]. The measurement methods are determined by experimental measurements and the assessment of the building factor (*BF*). The building factor is defined as the ratio of measured no-load loss of a transformer (in watts per kg) to the estimated value based on nominal steel core loss (Epstein or Single Sheet Test loss in watts per kg) [1]. The building factor depends on several parameters, such as the air gap, areas of overlapping joints and the size of the stacking holes [1,2,7,8], therefore empirical methods require a huge number of measurements [8]. Additionally, due to the continuous optimization of the technical properties of both magnetic materials and the core structure, measurements of the core losses of these distribution transformers should be updated [8]. However, empirical techniques are characterized by fast calculations as well as taking into account all parts of the core losses.

Core losses can also be determined based on equivalent magnetic circuits using analytical methods [9, 10]. The analytical methods are built on a semiempirical description of the different components of core losses: hysteresis losses, eddy-current losses, and excess losses, which are functions of frequency and maximum flux density. The no-load losses are calculated by the introduction of resistance to the overall equivalent circuit model of the transformer [9]. Analytical methods are effectively used to study inrush current, ferroresonance, transients, etc., and are relatively simple [9,10]. Most often analytical methods are applied in real operation analysis. Nevertheless, these methods cannot accurately estimate core losses, and commercial transformer design programs that use numerical or empirical methods are typically used [8].

Artificial intelligence methods, which are often based on neural networks, are also used to determine core losses. Neural networks are applied to estimate core losses as a function of basic design parameters [8,11,12]. The accuracy of these methods is commonly dependent on the correctness of the training of neural network sets [8]. Generally, neural networks are effective in predicting no-load losses of power transformers, but in [8] shows that there are cases where the estimation error is unacceptable after the completion of transformer construction.

Then numerical methods calculate no-load losses by solving Maxwell Equations with numerical techniques such as Finite Element Methods (FEM) [8,13,14]. FEM is a highly successful numerical tool for verification and optimization of new transformer designs as well as used materials [14]. The main issues of these methods are time-consuming calculations.

One of the empirical methods described in a previous paper [3] takes into account the mass m, grade of steel as core losses p and the extra losses factor k_p estimated through analysis of transformers series. The formula may be presented as follows:

$$\Delta P_{Fe} = k_p \, m \, p, \tag{1}$$

There is considered that the main effect on the extra losses factor, and thereby on no-load losses, may have core's corners. This is the region, where the magnetic flux changes the direction. The flux goes through the corner from the limb to the yoke or inversely. In regard to this, the direction of the magnetization of the sheet doesn't coincide with the rolling direction. The angle between these directions is named the anisotropy angle and its increase leads to a higher value of losses.

Table I shows data for selected transformers produced by Power Engineering Transformatory. It contains the power, the percent content of corners in the entire core mass and the extra losses factor. There are two values of k_p factor – first used for the calculation of losses and second recalculated from the no-load losses obtained in the test. The comparison of these two values is significant to develop a more accurate algorithm for the no-load losses calculations. The designer may modify the factor according to results from the analysis of measured losses.

The second purpose of the creation of the Table I was to check if there is a dependency between the content of corners and the extra losses factor. The dependency is not visible, hence the more complex analysis should be performed. That analysis should include e.g. the value of magnetic flux density, the grade of steel. Besides, more designs should be compared. Table I contains 19 units, though there are only three different designs. The dimensions of one of the cores from Table I are presented in Table II.

TABLE I. NO-LOAD LOSSES AND CORE EXTRA LOSSES FACTOR FOR DIFFERENT CONTENT OF CORNERS IN THE CORE

No.	Power	Content of corners in entire core mass	No-load losses		Core extra losses factor	
			calculated	measured	calculated	measured
-	MVA	%	W	W	%	%
1	16	26,9	7886	7970	15	16,1
2	16	26,9	7886	7960	15	16,2
3	25	28,7	11730	11678	17	16,5
4	25	28,7	11730	11397	17	13,6
5	25	28,7	11730	11832	17	18
6	25	28,7	11730	11560	17	15,3

7	25	28,7	11730	11539	17	15,1
8	25	28,7	11730	11370	17	13,4
8	25	28,7	11730	11405	17	13,8
10	25	28,7	11730	11265	17	12,3
11	25	28,7	11730	11714	17	16,8
12	25	28,7	11730	11452	17	14,2
13	25	28,7	11730	11507	17	14,7
14	25	28,7	11730	11206	17	11,8
15	25	28,7	11730	11392	17	13,6
16	25	28,7	11730	11376	17	13,4
17	25	28,7	11730	11183	17	11,5
18	40	27,59	13216	12831	17	13,6
19	40	27,59	13216	12855	17	13,8

The measured values of the no-load losses are mostly lower from calculated ones. That implies the real core extra losses factor to be lower than taken into calculations. This is different only for 16 MVA transformers with assumed factor for calculations equal to 15% and the one 25 MVA transformer. For the factor 17%, the real value recalculated base on the measured losses ranges mainly from 13% to 16%.

The variation of measured losses for the same design might be affected by accuracy in the production of these cores. Even though the design is the same, produced cores may not be identical. Moreover, the disassembly of the upper yoke before placing the windings on limbs, then the reassembly, may have an impact on losses.

III. THREE PHASE TRANSFORMER CORE

The object of a survey was a transformer core (Fig. 3 and Table II). Generally, the transformer structures at the corner joint are made as a butt-lap joint either mitred overlap joint - see Fig. 2. In this paper, we considered mitred overlap joint.

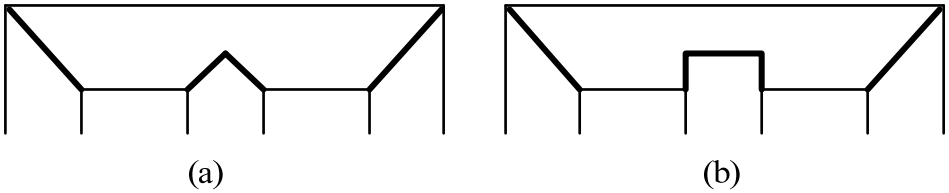

Figure 2. Different types of T-joins design: mitred 45°(a) and butt-lap 90° overlap joint (b)

Particularly, the corner of the core was the main concern as this is the area where the anisotropy occurs. The core lamination is made alternately. The layers of sheets are interlaced in the places where the columns are connected with the yokes, precisely in the corners and nodes. The most commonly used solution is the core's lamination with sheets cut angled at 45º. In such cores, the areas with different directions of rolling and magnetizing are smaller than in the case of cores laminated at the right angle. Hence the maximum anisotropy angle also equals 45º.

The examined core was made with lamination at 45º (Fig. 4). The chosen type of steel sheet was M080-23P5. The most significant parameters of this steel: the magnetic flux density at 800 A/m equals to 1,916 T and the typical core loss at 1,7 T (for 50 Hz) is 0,77 W/kg. All these parameters are catalog values specified for the direction of magnetization parallel to the direction of rolling. The values differ depending on the anisotropy angle. The impact of these variations on the magnetic flux density distribution was analysed in the paper.

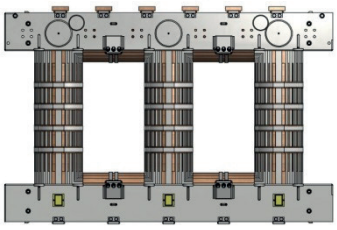

Figure 3. Assembly of the three-phase transformer core

TABLE II. DIMENSIONS OF THE EXEMPLARY CORE

Dimension	Value
Sheet thickness	0,23 mm
Core diameter	525 mm
Height	2456 mm
Width	2869 mm
Mass	15 200 kg

IV. SELECTED RESULTS

The distribution of the magnetic flux density in the core was modeled by the finite element method. The computation was performed in the Comsol Multiphysics software. Therefore to simplify the calculations, the 3D model contained a single limb and yoke (orange marking in Fig. 4). Moreover, there were only three steps in half of the core's cross-section. Although the real core contains typically more than 10 steps.

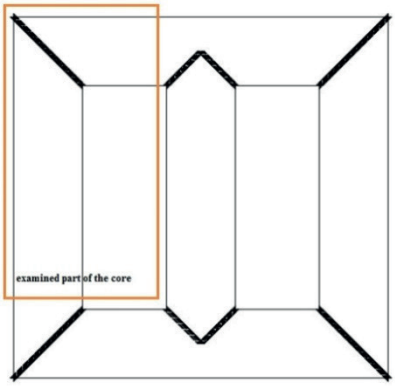

Figure 4. The view of the transformer's model

In the paper, two cases were examined. The first one didn't include different properties for different anisotropy angles (Fig. 5a). In the second case, the difference in properties was taken into account. The corner was divided into smaller elements, every 10º (Fig. 5b). This division enabled the implementation of the anisotropy in the model. The proper magnetization curve B(H) (Fig. 6) was applied to each part of the corner.

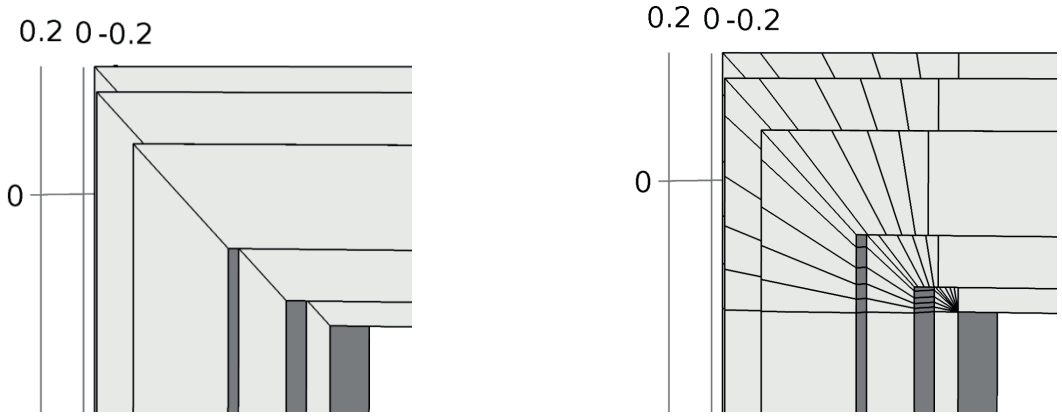

(a) (b)

Figure 5. Considered core models in FEM analysis: model 1(a), model 2 (b)

The curve for 0° corresponds with the one contained in the steel producer's catalogue. This curve was also implemented in case 1. The remaining curves were developed on the basis of the study included in [15]. The author of that paper describes the measurements of electrical steel. The results show dependency between the anisotropy angle and the magnetization curve, as well as core losses. According to this survey, the magnetic flux density decreases for a greater anisotropy angle (for the same value of the magnetic field).

The magnetic flux density and the magnetic field were calculated proportionally to values from the survey [15]. In order to measure parameters for different anisotropy angles, the sheet strips are cut at the proper angle relative to the rolling direction. On account of this survey, the authors made the assumption that as the anisotropy angle for M080-23P5 steel increases, the magnetic flux density will decrease by the same percentage as in the mentioned survey.

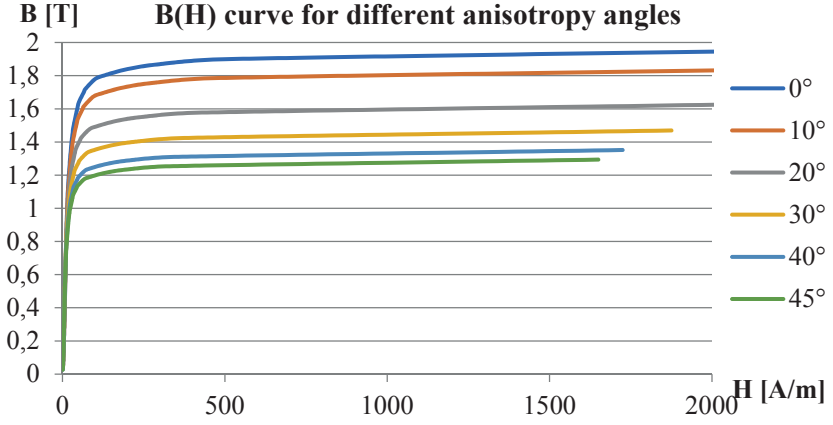

Figure 6. The magnetization curve for different anisotropy angle

In order to examine the distribution of the magnetic flux density, the constant value as a vector was applied to the ending surfaces of the yoke and the limb. The vector supplied to the yoke had a value of 1,7 T when to the limb it was -1,7 T. The condition is described by the formula:

$$-\boldsymbol{n} * \boldsymbol{B} = B_m, \tag{2}$$

where:

n – directional vector (normal),

B – magnetic flux density vector,

B_m – maximum magnetic flux density.

The results of the FEM calculations for both investigated cases are shown in Figure 7. In the yoke and the limb, where the direction of rolling is the same as the direction of magnetization, the magnetic flux density is constant and equal to 1,7 T. Instead, the value differs in the area of the corner. The more accurate distribution is presented in Figure 8. The surface showed in Fig. 8 is the diagonal cross-section of the corner. The magnetic flux density is greater closer to the inner part of the corner and lower closer to the outer part.

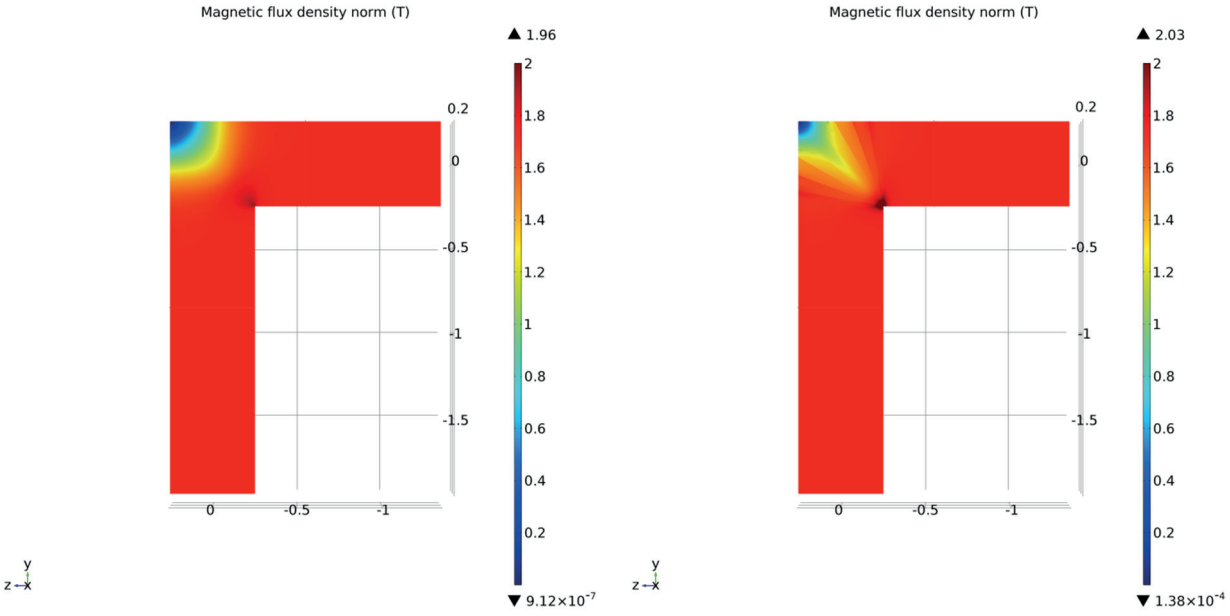

(a) (b)

Figure 7. The magnetic flux distribution for: model 1 (a), model 2 (b)

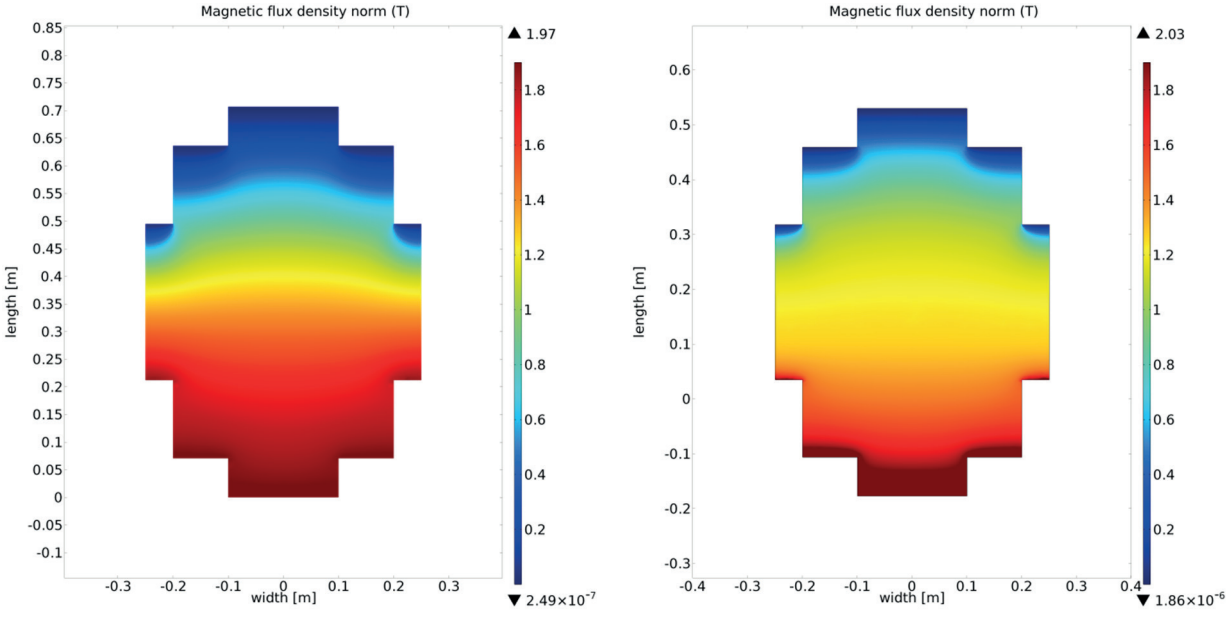

(a) (b)

Figure 8. The magnetic flux distribution in the corner: model 1 (a), model 2 (b)

Nonetheless, the distribution differs for two examined cases. In case 1 (Fig. 7a) the area of the lowest magnetic flux density is larger while the area of the highest is smaller. However, the minimum value is $9{,}12 \cdot 10^{-7}$ and the maximum value exceeding saturation is equal to 1,96 T. There should be emphasized that the increase of the magnetic flux density affects the increase of core losses and therefore no-load losses.

In view of this, the second case was analysed (Fig. 7b). Taking into account various magnetization curves for proper parts of the corner led to more precise results in the calculation. The difference between cases 1 and 2 is visible. The area of the magnetic flux up to 1 T is smaller while the region with the value above 1,8 T is wider. Furthermore, the range of approximately 1 T and 1,6 T is not placed around the outer corner as in case 1. That area extends through the diagonal of the corner. The extreme values are greater in this variant. The maximum value obtained in case 2 is 2,03 T and minimum $1{,}38 \cdot 10^{-4}$ T.

V. CONCLUSIONS

The aim of the paper was to observe the distribution of the magnetic flux density in the transformer's anisotropy core. Moreover, a short analysis of the no-load losses for different designs was performed. However, the analysis of calculated and measured values of the no-load losses allows assessing the correctness of the designing process. Obtaining comparable results is significant from the perspective of meeting the conditions set by the customer. Despite the fluctuation of the extra losses factor, all analysed transformers have losses below the required ones. Most measured values are lower about 1-5% than calculated. Observation of the relationship between the content of corners in the entire core mass and the extra losses factor should take into account more parameters. The magnetic flux density and the core loss for a particular grade of steel should be also considered.

Although there are several methods for calculating no-load losses, each requires a complex analysis of measured values. Real values should be taken into account during further development and improvement of algorithms.

The second part of the paper is dedicated to the distribution of magnetic flux density in the core. The results of the simulation show that in the corner the distribution is uneven. The implementation of different magnetization curves, resulting from the anisotropy angle, leads to obtaining a more accurate outcome. The distribution for model 2 is apparently different than for model 1. That knowledge is substantial for future studies.

The computations conducted in this paper will be developed in the future. It is planned to develop a method for calculating no-load losses using FEM. The impact of the varied distribution of the magnetic flux density will be included. Obtained results will show how much losses occur in the corner compared to other areas of the core. Moreover, the total no-load losses will be compared with the values calculated with formula 1. And also a comparison of this approach with that using an anisotropic magnetic permeability tensor will be carried out to determine the validity and accuracy of the proposed method.

VI. REFERENCES

[1] A. J. Moses, “Prediction of Core Losses of Three Phase Transformers from Estimation of the components Contributing to the Building Factor,” *Journal of Magnetism and Magnetic Materials*, Vol. 254-255, doi:10.1016/S0304-8853(02)00911-3, 2003, pp. 615- 617.

[2] E.G. teNyenhuis, R.S. Girgis, G.F. Mechler, Other factors contributing to the core loss performance of power and distribution transformers, IEEE Trans. Power Delivery, 16, 2001, pp. 648-653.

[3] J. Wojtkun; B. Bródka; D. Stachowiak, "The influence of core geometry on no-load losses of medium power transformers", *IEEE Conferences*, DOI: 10.1109/IIPHDW.2018.8388339, 2018, pp. 123-127.

[4] W. Mazgaj, A. Warzecha, “Influence of electrical steel sheet textures on their magnetization curves”, ARCHIVES OF ELECTRICAL ENGINEERING VOL. 62(3), DOI 10.2478/aee-2013-0034, 2013, pp. 425-437.

[5] F. Jiang, M. Rossi, G. Parent, “Anisotropy model for modern grain oriented electrical steel based on orientation distribution function”, AIP Advances 8, 056104 (2018); https://doi.org/10.1063/1.5006471.

[6] W. Pluta, „Angular properties of specific total loss components under axial magnetization in grain-oriented electrical steel”, IEEE Transactions on Magnetics, vol. 52, issue 4, no. 6300912, 2016.

[7] N. Ashbahani, I. Daut, Y.M. Irwan, "Building Factor of Grain-Oriented Silicon Iron (3% SiFe) with Different Thickness on 100kVA Three Phase Distribution Transformer Core", Advanced Materials Research, Vols. 488-489, 2012, pp. 537-541.

[8] P. S. Georgilakis, “Spotlight on Modern Transformer Design,” Springer-Verlag, New York, doi:10.1007/978-1-84882-667-0, 2009.

[9] M. Elleuch, M. Poloujadoff, “Analytical model of iron losses in power transformers,” IEEE Transactions on Magnetic, Vol. 39, No. 2, doi:10.1109/TMAG.2003.80859, 2003, pp. 973-980.

[10] J. Pedra, , F. Corcoles, , L Sainz, R. Lopez, “Harmonic nonlinear transformer modeling,” IEEE Transactions on Power Delivery, Vol. 19, 2004, pp. 884-890.

[11] C. Nussbaum, H. Pfutzner, Th. Booth, N. Baumgartinger, A. Ilo and M. Clabian, “Neural Networks for the Prediction of Magnetic Transformer Core Characteristics,” IEEE Transactions on Magnetic, Vol. 36, No. 1, 2000, pp. 313-329. doi:10.1109/20.822542.

[12] P. S. Georgilakis, N. D. Doulamis, A. D. Doulamis, N. D. Hatziargyriou, and S. D. Kollias, “A novel iron loss reduction technique for distribution transformers based on a combined genetic algorithm – neural network approach,” IEEE Transactions on Systems, Man and Cybernetics, Part C, Vol. 31, 2001, pp. 16-34.

[13] D. Koteras, Transformers with low core losses- field analysis and measurement verification, Opole University of Technology Publishing, Opole, 2015.

[14] M. A. Tsili, A. G. Kladas and P. S. Georgilakis, “Computer aided analysis and design of power transformers”, Elsevier Journal Computers in Industry, vol. 59, no. 4, 2008, pp. 338-350.

[15] E. Napieralska-Juszczyk, K. Komęza, “Modelowanie pola elektromagnetycznego w rdzeniach anizotropowych”, Monografie Politechniki Łódzkiej, Łódź, 2012.

ENERGIJA